

Feasibility of the Use of Time of Flight to Detect  
 $K_L \rightarrow \pi^0 \nu \bar{\nu}$  at Fermilab Main Injector

Shuji Mochida  
High Energy Physics Group  
Department of Physics at Osaka University

March 28, 1998

# Abstract

The main purpose of the kaons at the Main Injector (KAMI) proposed at Fermilab is to detect a rare decay,  $K_L \rightarrow \pi^0 \nu \bar{\nu}$ , in order to determine the origin of  $CP$  violation predicted in the Standard Model. The newly constructed Main Injector will provide a high intensity proton beam at 120 GeV, which will enable us to obtain higher signal acceptance and lower background level. Considering this benefit of KAMI, this paper presents an estimate of feasibility of signal detection by the use of time of flight measurement of kaons and their decay products.

# Acknowledgement

I would like to show my gratitude to all the people who were associated with my two year study at Osaka University and completion of this thesis. I am grateful to members of the KTeV collaboration, including Katsushi Arisaka at University of California, Los Angeles and Tsuyoshi Nakaya at the University of Chicago for their advice and instruction for my MC simulation.

I also owe a lot to the members of the Nagashima Group at Osaka University for the good companionship and encouragement. Daisuke Tatsumi, Kazunori Hanagaki, Takeo Kawasaki, Takayuki Yamaguchi, Masayoshi Sadamoto, Katsumi Senyo, Akira Kusano, Satoshi Hidaka, Masanori Sogo, Kazutaka Sumisawa, and Tomoki Takegai, have given me great deal of help to proceed my research. With Kiyoyuki Higuchi, Takahiro Houjo, Masato Kouyama, Keitaro Kurebayashi, Koji Mori, Jiro Ryuko, Hiroshi Yamada, and Makoto Yoshida, I shared good time on talking about physics and lead enjoyable research life. Further gratitude is given to Masato Takita, Masashi, Hazumi, Takanori Hara, and Ichiro Suzuki for their kind instruction of the basics of physics as well as computer skills. Sachiko Tsuzuki's help and support for my research life must also be mentioned here.

I would like to give my profound thankfulness to the dedicated work of instruction and advice of Taku Yamanaka for the completion of this thesis. His deep concern on physics and keen eyes on everything he sees to seek the essential part of nature gave me a great amount of inspiration. Finally, I would like to thank my adviser, Professor Yorikiyo Nagashima, for giving me a chance to work on a research in high energy physics. From his devotion to physics I learned the attitude of professional researcher, which would certainly affect the rest of my life.

# Contents

<b>1</b>	<b>Introduction</b>	<b>9</b>
1.1	$CP$ Violation . . . . .	9
1.2	Decay of $K_L \rightarrow \pi^0 \nu \bar{\nu}$ —a Key to Understanding the Origin of $CP$ Violation	10
1.2.1	CKM Matrix . . . . .	11
1.2.2	Decay of $K_L \rightarrow \pi^0 \nu \bar{\nu}$ . . . . .	12
1.3	$K_L \rightarrow \pi^0 \nu \bar{\nu}$ Detection . . . . .	14
1.3.1	$\pi^0 \rightarrow \gamma\gamma$ with Hermetic Veto . . . . .	14
1.3.2	$\pi^0$ Dalitz Decay . . . . .	14
1.3.3	Time of Flight . . . . .	15
1.4	Use of the Time of Flight Measurement at KAMI . . . . .	15
<b>2</b>	<b>Monte Carlo Simulation of the KAMI Experiment</b>	<b>16</b>
2.1	Neutral Beam from the Main Injector . . . . .	16
2.2	Detector . . . . .	16
2.2.1	CsI Calorimeter . . . . .	17
2.2.2	Photon Veto System . . . . .	18
2.2.3	Detector inefficiency . . . . .	19
2.3	Event Weighting Technique . . . . .	20
<b>3</b>	<b>Analysis without Time of Flight</b>	<b>22</b>
3.1	Background Decay Modes . . . . .	22
3.1.1	$K_L \rightarrow \pi^0 \pi^0$ . . . . .	22
3.1.2	$K_L \rightarrow \pi^0 \pi^0 \pi^0$ . . . . .	23
3.1.3	$\Lambda \rightarrow n \pi^0$ . . . . .	23
3.1.4	$K_L \rightarrow \gamma\gamma$ . . . . .	23
3.1.5	$nA \rightarrow \pi^0 A$ . . . . .	23
3.2	Event Selection . . . . .	23
3.2.1	Clustering . . . . .	23
3.2.2	Photon Veto . . . . .	24
3.2.3	Beam Axis Component of the Decay Vertex of $\pi^0$ . . . . .	24
3.2.4	Transverse Momentum of $\pi^0$ . . . . .	25

3.2.5	Total Energy of Gamma Clusters on the CsI Calorimeter . . . . .	25
3.3	The Number of $K_L \rightarrow \pi^0 \nu \bar{\nu}$ and Background Events . . . . .	25
<b>4</b>	<b>Time of Flight Measurement</b>	<b>32</b>
4.1	Kinematics and Method . . . . .	32
4.2	Time and Energy resolutions . . . . .	34
4.3	Cut on the $\pi^0$ Energy in the $K_L$ Center of Mass System . . . . .	34
4.3.1	$\beta$ Cut . . . . .	35
4.3.2	The Number of Events Observed for a Year . . . . .	36
4.4	Results with Different Conditions . . . . .	37
4.4.1	Energy Resolution . . . . .	37
4.4.2	Gamma Veto Inefficiency . . . . .	37
<b>5</b>	<b>Discussion</b>	<b>46</b>
5.1	$E_\pi^*$ Cut . . . . .	46
5.2	Required Inefficiency and Resolution to Make Use of Time of Flight . . .	47
5.2.1	Inefficiency . . . . .	47
5.2.2	Time Resolution . . . . .	47
5.2.3	Energy Resolution . . . . .	48
5.3	$K_L$ Momentum . . . . .	48
5.4	Feasibility of the time of flight measurement at KAMI . . . . .	49
<b>6</b>	<b>Conclusion</b>	<b>53</b>

# List of Figures

1.1	The unitarity triangle . . . . .	12
1.2	The Z penguin and W-box diagrams which contribute to the decay $K_L \rightarrow \pi^0 \nu \bar{\nu}$ . . . . .	13
2.1	The detector geometry used for the Monte Carlo simulation . . . . .	17
2.2	Photon detection inefficiency as a function of energy in lead-scintillator detectors quoted from Ref. [7]. The open circles, the cross points, and the dot points show the inefficiency due to the sampling effect, the photonuclear interaction, and their sum, respectively. . . . .	21
3.1	The beam axis component of the decay vertex of $\pi^0$ for (a) $K_L \rightarrow \pi^0 \nu \bar{\nu}$ , (b) $K_L \rightarrow \pi^0 \pi^0$ , and (c) $K_L \rightarrow \pi^0 \pi^0 \pi^0$ . The shaded area is discarded by the condition, $152 < z_{vtx} < 171$ m. . . . .	27
3.2	The transverse momentum distribution for (a) $K_L \rightarrow \pi^0 \nu \bar{\nu}$ , (b) $K_L \rightarrow \pi^0 \pi^0$ , and (c) $K_L \rightarrow \pi^0 \pi^0 \pi^0$ . The shaded area is discarded by the condition, $p_t > 150$ MeV. . . . .	28
3.3	The total energy deposit in the CsI clusters for (a) $K_L \rightarrow \pi^0 \nu \bar{\nu}$ , (b) $K_L \rightarrow \pi^0 \pi^0$ , and (c) $K_L \rightarrow \pi^0 \pi^0 \pi^0$ . The shaded area is discarded by the condition, $E_t > 5$ GeV. . . . .	29
3.4	The z vertex and $P_t$ distributions for (a) $K_L \rightarrow \pi^0 \nu \bar{\nu}$ (b) $K_L \rightarrow \pi^0 \pi^0$ , and (c) $K_L \rightarrow \pi^0 \pi^0 \pi^0$ events from a Monte Carlo simulation . . . . .	30
3.5	The integrated number of events expected for one year operation after all cuts in Table 3.2 had been made is shown for (a) $K_L \rightarrow \pi^0 \nu \bar{\nu}$ , (b) $K_L \rightarrow \pi^0 \pi^0$ , and (c) $K_L \rightarrow \pi^0 \pi^0 \pi^0$ at $E_t = 20$ GeV. . . . .	31
4.1	$E_\pi^*$ distribution with no smearing. The above figure shows the extended distribution of $\pi^0$ coming from $K_L \rightarrow \pi^0 \nu \bar{\nu}$ while the bottom one indicates the sharp peak of $\pi^0$ from $K_L \rightarrow \pi^0 \pi^0$ . The small histograms in the $K_L \rightarrow \pi^0 \pi^0$ figure are due to gammas coming from different $\pi^0$ 's. . . . .	33
4.2	Energy resolution vs. momentum for electrons. The contribution from momentum resolution is removed [11]. . . . .	35

- 4.3  $E_\pi^*$  distribution for  $K_L \rightarrow \pi^0 \nu \bar{\nu}$  with smearing effects. (a) $\sigma_T = 500$  ps, (b) $\sigma_T = 400$  ps, (c) $\sigma_T = 300$  ps, (d) $\sigma_T = 200$  ps, (e) $\sigma_T = 100$  ps, and (f) $\sigma_T = 50$  ps. The solid line represents the  $K_L$  momentum to be less than 120 GeV/c, while dashed line for 50 GeV/c, half-dotted line for 20 GeV/c, and dotted line for 10 GeV/c. Because the distribution of initial  $K_L$  momentum for survived events stretches from  $p_{K_L} = 5$  GeV to  $p_{K_L} = 50$  GeV for  $K_L \rightarrow \pi^0 \nu \bar{\nu}$  and from  $p_{K_L} = 5$  GeV to  $p_{K_L} = 30$  GeV for  $K_L \rightarrow \pi^0 \pi^0$ , there can be seen overlap of  $p_{K_L} < 120$  GeV and  $p_{K_L} < 50$  GeV plots for  $K_L \rightarrow \pi^0 \nu \bar{\nu}$  and  $p_{K_L} < 120$  GeV  $p_{K_L} < 50$  GeV, and  $p_{K_L} < 20$  GeV plots for  $K_L \rightarrow \pi^0 \pi^0$ . . . . . 38
- 4.4  $E_\pi^*$  distribution for  $K_L \rightarrow \pi^0 \pi^0$  with smearing effects. (a) $\sigma_T = 500$  ps, (b) $\sigma_T = 400$  ps, (c) $\sigma_T = 300$  ps, (d) $\sigma_T = 200$  ps, (e) $\sigma_T = 100$  ps, and (f) $\sigma_T = 50$  ps. The solid line represents the  $K_L$  momentum to be less than 120 GeV/c, while dashed line for 50 GeV/c, half-dotted line for 20 GeV/c, and dotted line for 10 GeV/c. Because the distribution of initial  $K_L$  momentum for survived events stretches from  $p_{K_L} = 5$  GeV to  $p_{K_L} = 50$  GeV for  $K_L \rightarrow \pi^0 \nu \bar{\nu}$  and from  $p_{K_L} = 5$  GeV to  $p_{K_L} = 30$  GeV for  $K_L \rightarrow \pi^0 \pi^0$ , there can be seen overlap of  $p_{K_L} < 120$  GeV and  $p_{K_L} < 50$  GeV plots for  $K_L \rightarrow \pi^0 \nu \bar{\nu}$  and  $p_{K_L} < 120$  GeV  $p_{K_L} < 50$  GeV, and  $p_{K_L} < 20$  GeV plots for  $K_L \rightarrow \pi^0 \pi^0$ . . . . . 39
- 4.5 The distribution of calculated  $\beta$  is shown for different time resolutions,  $\sigma_T$ , to be (a)500 ps, (b)400 ps, (c)300 ps, (d)200 ps (e) 100 ps, and (f)50 ps. The shaded area shows  $\beta < 1$  region which is used for  $E_\pi^*$  calculation. The number within each plot shows the fraction of events satisfying  $\beta \geq 1$ . 40
- 4.6 The number of events expected for  $K_L \rightarrow \pi^0 \nu \bar{\nu}$  for one year operation is shown as a function of the cut on  $E_\pi^*$ . (a) $\sigma_T = 500$  ps, (b) $\sigma_T = 400$  ps, (c) $\sigma_T = 300$  ps, (d) $\sigma_T = 200$  ps, (e) $\sigma_T = 100$  ps, and (f) $\sigma_T = 50$  ps. The solid line represents the  $K_L$  momentum to be less than 120 GeV/c, while dashed line for 50 GeV/c, half-dotted line for 20 GeV/c, and dotted line for 10 GeV/c. . . . . 41
- 4.7 The number of events expected for  $K_L \rightarrow \pi^0 \pi^0$  for one year operation is shown as a function of the cut on  $E_\pi^*$ . (a) $\sigma_T = 500$  ps, (b) $\sigma_T = 400$  ps, (c) $\sigma_T = 300$  ps, (d) $\sigma_T = 200$  ps, (e) $\sigma_T = 100$  ps, and (f) $\sigma_T = 50$  ps. The solid line represents the  $K_L$  momentum to be less than 120 GeV/c, while dashed line for 50 GeV/c, half-dotted line for 20 GeV/c, and dotted line for 10 GeV/c. . . . . 42

4.8	The number of events expected for $K_L \rightarrow \pi^0 \nu \bar{\nu}$ for one year operation is shown as a function of the cut on $E_\pi^*$ . A smaller $\sigma_E$ in equation (4.6) is used here. (a) $\sigma_T = 500$ ps, (b) $\sigma_T = 400$ ps, (c) $\sigma_T = 300$ ps, (d) $\sigma_T = 200$ ps, (e) $\sigma_T = 100$ ps, and (f) $\sigma_T = 50$ ps. The solid line represents the $K_L$ momentum to be less than 120 GeV/c, while dashed line for 50 GeV/c, half-dotted line for 20 GeV/c, and dotted line for 10 GeV/c. . . . .	43
4.9	The number of events expected for $K_L \rightarrow \pi^0 \pi^0$ for one year operation is shown as a function of the cut on $E_\pi^*$ . A smaller $\sigma_E$ in equation (4.6) is used here. (a) $\sigma_T = 500$ ps, (b) $\sigma_T = 400$ ps, (c) $\sigma_T = 300$ ps, (d) $\sigma_T = 200$ ps, (e) $\sigma_T = 100$ ps, and (f) $\sigma_T = 50$ ps. The solid line represents the $K_L$ momentum to be less than 120 GeV/c, while dashed line for 50 GeV/c, half-dotted line for 20 GeV/c, and dotted line for 10 GeV/c. . . . .	44
4.10	The number of events expected for $K_L \rightarrow \pi^0 \pi^0$ for one year operation is shown as a function of the cut on $E_\pi^*$ with photon veto counters of poorer performance. (a) $\sigma_T = 500$ ps, (b) $\sigma_T = 400$ ps, (c) $\sigma_T = 300$ ps, (d) $\sigma_T = 200$ ps, (e) $\sigma_T = 100$ ps, and (f) $\sigma_T = 50$ ps. The solid line represents the $K_L$ momentum to be less than 120 GeV/c, while dashed line for 50 GeV/c, half-dotted line for 20 GeV/c, and dotted line for 10 GeV/c. . . . .	45
5.1	Probability that the $K_L \rightarrow \pi^0 \pi^0$ background can fluctuate to more than the total number of $K_L \rightarrow \pi^0 \nu \bar{\nu}$ and $K_L \rightarrow \pi^0 \pi^0$ , is shown as a function of $E_\pi^*$ . (a) $\sigma_T = 500$ ps, (b) $\sigma_T = 400$ ps, (c) $\sigma_T = 300$ ps, (d) $\sigma_T = 200$ ps, (e) $\sigma_T = 100$ ps, and (f) $\sigma_T = 50$ ps. . . . .	50
5.2	The probability that a low energy photon from the $K_L \rightarrow \pi^0 \pi^0$ decay is not vetoed is shown. Energy distribution of gammas hitting (a)Vacuum Veto Counter (PV), (b)Back Anti-In, (c)Back Anti-Out, for the $K_L \rightarrow \pi^0 \pi^0$ background events. The cuts described in Chapter 3 have been imposed.	51
5.3	With low initial momentum, $K_L \rightarrow \pi^0 \pi^0$ events appear due to low energy of photons. Figures (a) and (b) show the momentum distribution of initial $K_L$ 's and weighted number of events. Figures (c) and (d) represent the corresponding number of accumulated events for one year, respectively. .	52

# List of Tables

2.1	Detector inefficiencies used for background studies of $K_L \rightarrow 2\pi^0$ decays. Each notation is defined as MA = Mask Anti, PV = Photon Veto, and BA = Back Anti. The BA-In is the 15 cm $\times$ 15 cm square central region of BA, surrounded by the BA-Out region which is set to have infinite area. The CsI calorimeter is categorized into three sections. 15 cm $\times$ 15 cm beam hole is surrounded by the 60 cm $\times$ 60 cm CsI-In region, which is inside the 120 cm $\times$ 120 cm CsI-Mid region. Outmost part is defined as the CsI-Out region which has 190 $\times$ 190 cm <sup>2</sup> . . . . .	19
3.1	The fusion separation criteria in the CsI calorimeter used for studying the MC simulation. The decision is based on the distance between two photons. CsI-In, Mid, and Out are the notations defined in Table 2.1. . .	24
3.2	Cuts used in the MC simulation . . . . .	25
4.1	The ratio of events which passed the requirement $\beta < 1$ . . . . .	36

# Chapter 1

## Introduction

The existence of symmetry principles in physics had been speculated as a manifestation of underlying beauty of order of the universe. From Newtonian mechanics to quantum mechanics, symmetry principles, connected with conservation laws, have provided us economical but elegant ways of looking at the nature. The law of right-left symmetry, associated with parity conservation, and invariance in charge conjugation operation, the two discrete symmetry laws which gained importance in quantum mechanics, had also been assumed to hold in subatomic world of physics. In this context, the breakdown of the combination of charge and parity symmetry in kaon decay, following parity violation discovered in weak interactions, had given us great impact on our view of the nature. At the same time, however, the discovery opened our eyes toward a new framework of physics. Afterwards, efforts have been paid to establish a model which incorporates the  $CP$  violation.

After about three decades since the  $CP$  breaking observation, so called the Standard Model has become believed to be the most probable candidate for the full description of elementary particle physics. Recent attention has been focused upon the complete determination of the parameters introduced in this scheme. In this respect, the rare kaon decay,  $K_L \rightarrow \pi^0 \nu \bar{\nu}$ , has gained a key role for the determination of the parameters. We will observe the underlying physics and detection method of this decay mode in this chapter.

### 1.1 $CP$ Violation

It is known that  $K$  mesons have two eigenstates: the longer-lived kaons,  $K_L$ , whose lifetime is  $5.2 \times 10^{-8}$  seconds, and the shorter-lived kaons,  $K_S$ , which have lifetime of  $0.89 \times 10^{-10}$  seconds. The  $K_L$  decays to three pions, which form  $CP$  odd state, while the shorter-lived kaons decay to two pions in  $CP$  even state.

The combination of charge conjugation and parity transformation changes  $K^0$  into

$\bar{K}^0$ , and vice versa:

$$CP|K^0\rangle = |\bar{K}^0\rangle, \quad (1.1)$$

$$CP|\bar{K}^0\rangle = |K^0\rangle. \quad (1.2)$$

(We use a conventional phase definition, and currently neglect the small effect of  $CP$  violation.)

The eigenvalues and eigenstates of  $CP$  are described as:

$$|K_1\rangle = \frac{1}{\sqrt{2}} [ |K^0\rangle + |\bar{K}^0\rangle ] \quad (CP = +1), \quad (1.3)$$

$$|K_2\rangle = \frac{1}{\sqrt{2}} [ |K^0\rangle - |\bar{K}^0\rangle ] \quad (CP = -1). \quad (1.4)$$

It had been believed from  $CP$  consistency that  $|K_2\rangle$  was responsible for the three pion decays while  $|K_1\rangle$  was for two pion decays.

In 1964, Cronin and Fitch, *et al.*, observed that the longer-lived kaons decayed to two pions [1]. This suggests that  $CP$  odd long-lived kaons,  $K_L$ , decays into  $CP$  even mode, and  $CP$  is not conserved in this decay.

This phenomenon can be explained if  $K_L$  is actually composed not only of  $|K_2\rangle$  but also with a slight mixture of  $|K_1\rangle$ :

$$|K_L\rangle = \frac{1}{\sqrt{1+\epsilon^2}} [ |K_2\rangle + \epsilon|K_1\rangle ], \quad (1.5)$$

Such a mechanism where the two-pion decay of the  $K_L$  is due to a small contribution from  $K_1$  is called indirect  $CP$  violation. However,  $CP$  can be violated if  $K_2$  in equation (1.5) decays to two  $\pi^0$ 's. If  $K_2$  directly decays to two pions, we can say that the  $CP$  is directly violated.

## 1.2 Decay of $K_L \rightarrow \pi^0 \nu \bar{\nu}$ —a Key to Understanding the Origin of $CP$ Violation

There are currently two frameworks to look at  $CP$  violation. One is the Standard Model, which incorporates electromagnetic, weak, and strong interactions into a single scheme. It has a mechanism to introduce  $CP$  violation, including the direct  $CP$  violation. The other is Superweak Model, which proposes a new  $\Delta S = 2$  interaction in  $K^0 - \bar{K}^0$  mixing to cause only the indirect  $CP$  violation. A detection of a single event of a direct  $CP$  violating decay can exclude the possibility of the Superweak Model and establishes the validity of the Standard Model.

### 1.2.1 CKM Matrix

In the Standard Model picture, direct  $CP$  violation is connected to the framework of quark mixing presented by Cabbibo, Koboyashi, and Maskawa [2]. In this theory, direct  $CP$  violation stems from the consequence of a three generation model.

The charged current in weak interaction can be written as:

$$J^\mu = \begin{pmatrix} \bar{u} & \bar{c} & \bar{t} \end{pmatrix} \frac{\gamma^\mu(1 - \gamma^5)}{2} U \begin{pmatrix} d \\ s \\ b \end{pmatrix}. \quad (1.6)$$

The matrix  $U$ , introduced by Kobayashi and Maskawa, tells us the coupling of up and down type quarks:

$$U = \begin{pmatrix} U_{ud} & U_{us} & U_{ub} \\ U_{cd} & U_{cs} & U_{cb} \\ U_{td} & U_{ts} & U_{tb} \end{pmatrix}. \quad (1.7)$$

The  $3 \times 3$  unitary matrix  $U$  can be represented by 4 parameters, with 5 arbitrary phases left aside. Of 4 parameters, 3 are real parameters and 1 is complex phase factor,  $e^{i\delta}$ , which accounts for the  $CP$  violation.

Wolfenstein parameterized the matrix components as follows [3]:

$$U = \begin{pmatrix} 1 - \frac{\lambda^2}{2} & \lambda & A\lambda^3(\rho - i\eta) \\ -\lambda & 1 - \frac{\lambda^2}{2} & A\lambda^2 \\ A\lambda^3(1 - \rho - i\eta) & -A\lambda^2 & 1 \end{pmatrix}. \quad (1.8)$$

From the unitarity condition, we have

$$U_{ub}^* U_{ud} + U_{cb}^* U_{cd} + U_{tb}^* U_{td} = 0, \quad (1.9)$$

yielding,

$$1 + \frac{U_{td} U_{tb}^*}{U_{cd} U_{cb}^*} = -\frac{U_{ud} U_{ub}^*}{U_{cd} U_{cb}^*} \equiv \bar{\rho} + i\bar{\eta}. \quad (1.10)$$

This relation determines the unitarity triangle illustrated in Fig. 1.1. Here,  $\bar{\rho} = \rho(1 - \lambda^2/2)$  and  $\bar{\eta} = \eta(1 - \lambda^2/2)$ .

The determination of the parameters shown in Fig. 1.1 is one of the primary goals of particle physics of today. As we will see, measurement of the branching ratio of rare  $CP$  violating decays determines the height of the triangle, and consequently tests the CKM scheme of quark interaction.

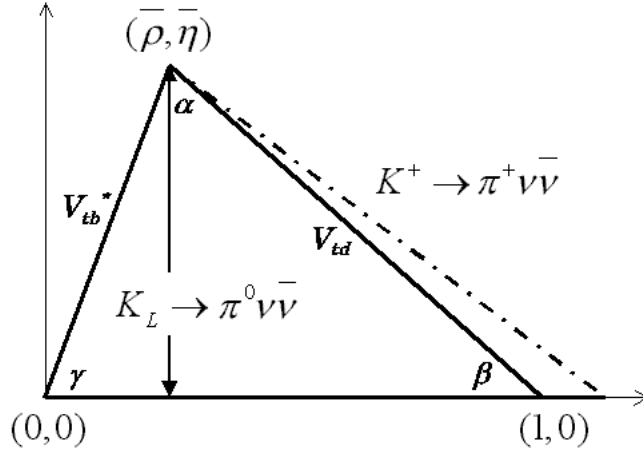


Figure 1.1: The unitarity triangle

### 1.2.2 Decay of $K_L \rightarrow \pi^0 \nu \bar{\nu}$

The observation of a rare decay  $K_L \rightarrow \pi^0 \nu \bar{\nu}$  is a good window to confirm the validity of the Standard Model theory. As shown in Fig. 1.2, this decay is governed by short-distance transition current and occurs almost entirely from the direct  $CP$  violation.

The amplitude for  $K_L \rightarrow \pi^0 \nu \bar{\nu}$  can be written as

$$A(K_L \rightarrow \pi^0 \nu \bar{\nu}) = \frac{1}{\sqrt{1 + \epsilon^2}} \left[ A(K_2 \rightarrow \pi^0 \nu \bar{\nu}) + \epsilon A(K_1 \rightarrow \pi^0 \nu \bar{\nu}) \right], \quad (1.11)$$

or

$$A(K_L \rightarrow \pi^0 \nu \bar{\nu}) = \frac{1}{\sqrt{2(1 + \epsilon^2)}} \left[ (1 + \epsilon) A(K^0 \rightarrow \pi^0 \nu \bar{\nu}) - (1 - \epsilon) A(\bar{K}^0 \rightarrow \pi^0 \nu \bar{\nu}) \right], \quad (1.12)$$

using equations (1.3) and (1.4). From the matrix expressions (1.7) and (1.8),

$$A(K_L \rightarrow \pi^0 \nu \bar{\nu}) \propto V_{td}^* V_{ts} - V_{ts}^* V_{td} \sim 2i\eta. \quad (1.13)$$

Thus, we can see that the branching ratio of  $K_L \rightarrow \pi^0 \nu \bar{\nu}$  is proportional to  $\eta^2$ , and determines the height of the unitarity triangle in Fig. 1.1.

The branching ratio can be calculated as

$$\begin{aligned} BR(K_L \rightarrow \pi^0 \nu \bar{\nu}) &= 1.94 \times 10^{-10} \eta^2 A^4 \chi^2(x) \\ &= 3.0 \times 10^{-11}, \end{aligned} \quad (1.14)$$

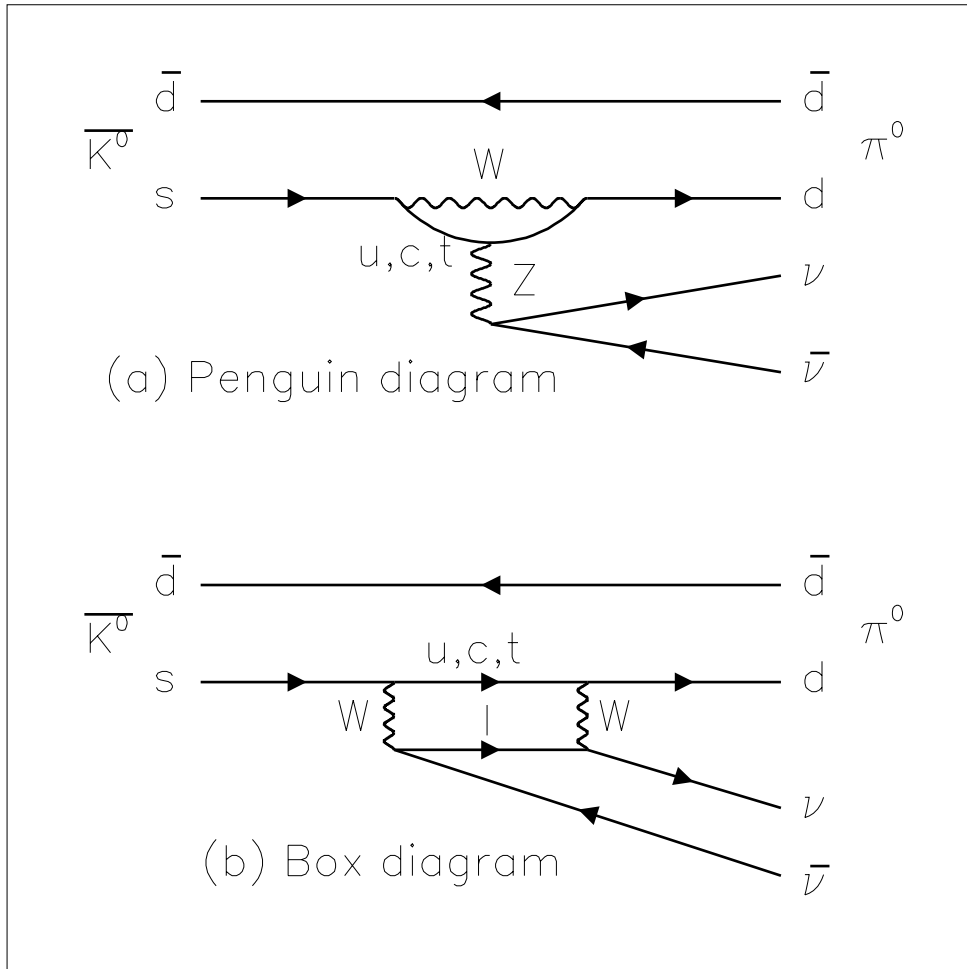


Figure 1.2: The  $Z$  penguin and  $W$ -box diagrams which contribute to the decay  $K_L \rightarrow \pi^0 \nu \bar{\nu}$

where  $x = m_t/m_W$ ,  $\chi \sim x^{1.2}$ , and  $A$  is a CKM parameter in Wolfenstein parameterization of equation (1.8) [4, 5].

### 1.3 $K_L \rightarrow \pi^0 \nu \bar{\nu}$ Detection

Of the three decay products of  $K_L \rightarrow \pi^0 \nu \bar{\nu}$ , only  $\pi^0$  is the observable particle. Our primary goal is to detect  $\pi^0$  which is consistent with the decay of  $K_L \rightarrow \pi^0 \nu \bar{\nu}$ . Several methods to detect such  $\pi^0$ 's are mentioned below.

#### 1.3.1 $\pi^0 \rightarrow \gamma\gamma$ with Hermetic Veto

Since almost 99 % of  $\pi^0$ 's decay into two  $\gamma$ 's, the detection of  $K_L \rightarrow \pi^0 \nu \bar{\nu}$  means finding  $2\gamma$ 's corresponding to a  $\pi^0$  decay. After vetoing all the charged particles, our main task is to veto neutral decay modes which produce two or more gammas. Such backgrounds include  $K_L \rightarrow \pi^0 \pi^0$ ,  $K_L \rightarrow \pi^0 \pi^0 \pi^0$ ,  $K_L \rightarrow \gamma\gamma$ ,  $K_L \rightarrow \pi^0 \gamma\gamma$ , and  $\Lambda \rightarrow n\pi^0$ . For  $K_L \rightarrow \gamma\gamma$  and  $\Lambda \rightarrow n\pi^0$ , we can assign a kinematic constraint on the obtained energy and position of the two gammas. In order to restrict the number of gammas to be two, hermeticity of the photon veto counter is required.

The KTeV experiment at Fermi National Accelerator Laboratory (FNAL) searched for  $K_L \rightarrow \pi^0 \nu \bar{\nu}$  for the first time using  $\pi^0 \rightarrow \gamma\gamma$ . Even with its non-hermetic gamma veto, it obtained a preliminary upper limit on the branching ratio of  $1.8 \times 10^{-6}$  with the 90 % confidence level [6].

KEK (High Energy Accelerator Research Organization in Japan) has a plan to use 12 GeV proton beam to detect  $K_L \rightarrow \pi^0 \nu \bar{\nu}$  by surrounding the decay region with a hermetic veto counter to reduce contributions from background gammas [7]. Expected single event sensitivity for 84 day operation is  $5.4 \times 10^{-10}$ .

At FNAL, a newly built Main Injector will provide high intensity proton beam at 120 GeV. The new KAMI (kaons at the Main Injector) experiment will utilize this beam to produce  $K_L$ 's. The typical momentum of  $K_L$  is 13 GeV/c. This high energy kaon beam gives us several advantages over other experimental sites. First of all, gammas from  $K_L \rightarrow \pi^0 \nu \bar{\nu}$  are boosted forward, increasing geometrical acceptance of  $K_L \rightarrow \pi^0 \nu \bar{\nu}$  signal detection. Secondly, generated photons have higher energies than those available at other two sites, which makes it easier to veto background events. Consequently, we can expect that higher momentum of  $K_L$  beam can lower the relative number of background events to the signal events.

#### 1.3.2 $\pi^0$ Dalitz Decay

Another way of detecting  $\pi^0$ 's consistent with decay  $K_L \rightarrow \pi^0 \nu \bar{\nu}$  is to find electron-positron pairs produced in the dalitz decay of  $\pi^0$ . This method has an advantage that we can detect the electron and positron tracks found by tracking chamber and use them

to fully reconstruct the  $\pi^0$  mass and decay vertex. However, the trade-off here is its small branching fraction (1.2 %) of the Dalitz decay and a low acceptance to collect low mass  $e^+e^-$  tracks. Therefore, this method will not be able to see  $K_L \rightarrow \pi^0\nu\bar{\nu}$  even at KAMI. E799-I at FNAL searched for the decay by utilizing this Dalitz decay and set an upper limit on branching ratio of less than  $5.8 \times 10^{-5}$  with the 90 % confidence level [8].

### 1.3.3 Time of Flight

Brookhaven National Laboratory (BNL) is proposing to measure the time of flight of  $K_L$  and reconstruct  $\pi^0$  momentum in  $K_L$  center of mass system [9]. The purpose is to reduce background from  $K_L \rightarrow \pi^0\pi^0$  which has a monochromatic  $\pi^0$  momentum in the center of mass system of  $K_L$ . A 24 GeV proton beam bunched in 130 ps wide buckets hits platinum target with 45 degrees to produce a  $K_L$  beam. The low momentum  $K_L$  beam, 700 MeV/c on average, makes the measurement of  $K_L$  momentum easier. However, at such a low momentum, the produced gammas have low energy deposit on veto counters, making their detection harder. The expected single event sensitivity for 1 year operation at BNL is  $8.2 \times 10^{-13}$ .

## 1.4 Use of the Time of Flight Measurement at KAMI

Combination of low inefficiency gamma veto and time of flight may be an effective way to increase signal ratio to its background events. Although, high energy  $K_L$ 's have  $\beta \sim 1$ , and thus make the time of flight measurement harder, the longer flight path of  $K_L$  in KAMI could compensate for that effect. The fact that the distance between the target and the decay region is longer in KAMI than that in BNL motivates us to use the measurement of time of flight to reconstruct event by event the energy of  $\pi^0$ 's in the center of mass frame of  $K_L$ . Utilization of time of flight plus good efficiency of photon veto in KAMI might enable us to attain better ratio of  $K_L \rightarrow \pi^0\nu\bar{\nu}$  events to other background events. In the following, we will study how the number of  $K_L \rightarrow \pi^0\nu\bar{\nu}$  and its background events depend on time and energy resolution in the KAMI detector. Possibility of using less efficient photon veto detectors is also argued.

# Chapter 2

## Monte Carlo Simulation of the KAMI Experiment

At Fermilab, an experiment to detect the decay,  $K_L \rightarrow \pi^0 \nu \bar{\nu}$ , and measure its branching ratio is planned to utilize the newly built Main Injector. The high intensity beam yielded from the Main Injector is expected to give us good sensitivity for  $K_L \rightarrow \pi^0 \nu \bar{\nu}$ .

In this chapter, we will first take a look at the new beam from the Main Injector and the KAMI spectrometer. Description of the Monte Carlo simulation will then follow the detector explanation.

### 2.1 Neutral Beam from the Main Injector

The Main Injector is currently constructed tangent to the Fermilab Tevatron main ring in order to improve the proton intensity by a factor of two to three. It can provide  $3 \times 10^{13}$  protons at 120 GeV every 2.9 seconds with a 1.0 second flat top.

In the KAMI experiment, a proton beam from the Main Injector will be directed on a beryllium-oxide target to produce kaons. The targetting angle is set to be 24 mrad to reduce neutron flux. The secondary beam is collimated to the solid angle of  $0.6 \text{ mrad} \times 0.6 \text{ mrad}$ . In order to simulate the neutral kaon beam generation, the standard KAMI Monte Carlo simulation software was used. Kaon decays were generated between 146 m and 186 m from the target, and between 5 GeV and 120 GeV in momentum. The number of  $K_L$  decays in this range is estimated to be  $2.8 \times 10^6$  per  $3 \times 10^{13}$  incident protons. The momentum distribution is generated according to the Malensek parameterization [10].

### 2.2 Detector

The geometrical detector configuration used in the MC simulation is shown in Fig. 2.1. Hereafter, the beam axis is referred to as “z-axis”, being equal to zero at the target

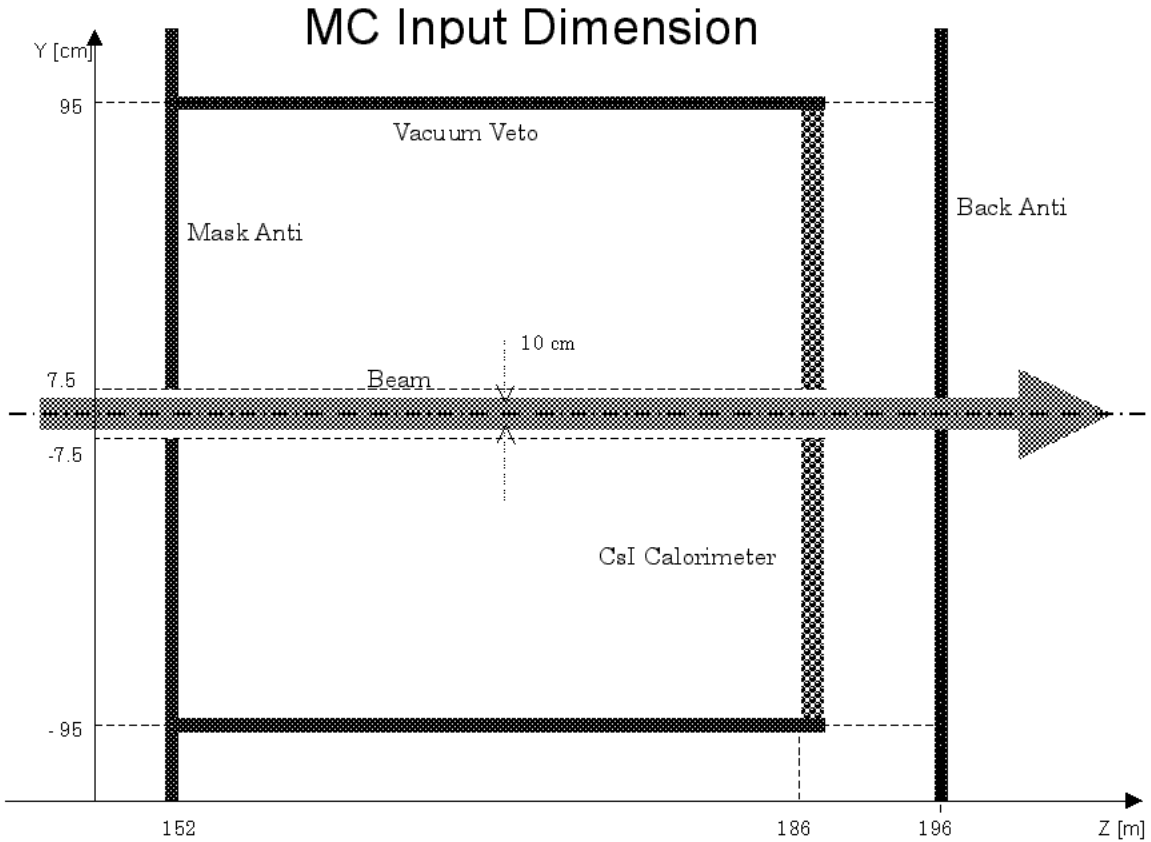


Figure 2.1: The detector geometry used for the Monte Carlo simulation

position.  $y$ -axis and  $x$ -axis are defined perpendicular to the  $z$ -axis.

The Mask Anti is placed at  $z = 152$  m, 36 m upstream of the CsI calorimeter and defines upstream decay region. Fiducial volume is covered by Vacuum Veto counter, stretching from  $z = 152$  m to  $z = 186$  m. At  $z = 186$  m, CsI calorimeter resides to detect photon energies. The Back Anti stands at 196 m downstream of the target to veto gammas coming through the beam hole. The area of the calorimeter is set to be  $190 \text{ cm} \times 190 \text{ cm}$ . We assumed the infinite area of the Mask Anti and the Back Anti.

Each of the detector component is briefly described in the following subsections.

### 2.2.1 CsI Calorimeter

The MC simulation for this study assumed that we utilize the CsI calorimeter for KTeV experiment. The detector consists of 3100 pure CsI crystals which are stacked in a  $1.9 \text{ m} \times 1.9 \text{ m} \times 27$  radiation length (50 cm) square with a  $15 \text{ cm} \times 15 \text{ cm}$  beam hole in the

center to avoid radiation damage from the intensive beam. The advantages of using pure crystals of CsI are their radiation hardness, good response time, and high light output to provide good energy resolution.

## 2.2.2 Photon Veto System

$K_L \rightarrow \pi^0\pi^0$  or  $K_L \rightarrow \pi^0\pi^0\pi^0$  decays can have more than two gammas which miss CsI calorimeter hits. The photon veto detectors serve the vital role in suppressing the number of such background events and must have as high efficiency as possible to attain our goal to detect the decay,  $K_L \rightarrow \pi^0\nu\bar{\nu}$ . The veto counters are sampling calorimeters composed of alternating layers of scintillating materials and stopping materials.

### Mask Anti

In order to reject background events from the region upstream of the decay volume, a 190 cm  $\times$  190 cm photon veto detector, called the Mask Anti (MA), is placed upstream end of the decay volume. This counter also vetoes gammas produced in the decay region. The Mask Anti has a 15 cm  $\times$  15 cm hole in the center to allow passage of the kaon beam.

### Vacuum Veto Counter

For capturing photons escaping the calorimeter, a hermetic gamma veto counter is required to cover the decay region. In the simulation, we assumed a 1.9 m  $\times$  1.9 m box covering the 34 m decay region between the Mask Anti and the CsI calorimeter. Vacuum veto counter, as well as the Mask Anti, is composed of alternate layers of lead and plastic scintillators. In order to suppress background level of  $K_L \rightarrow \pi^0\pi^0$ , high efficiency is required in order not to miss gammas from such background events.

### Back Anti

Identification of photons and neutrons passing through the hole in the calorimeter requires the beam hole veto counter, called the Back Anti (BA). The Back Anti is placed downstream of the calorimeter and detects photons which pass through the calorimeter hole. Since this counter is expected to receive 200 to 500 MHz of neutron interactions, a very fast, radiation hard material is necessary. We will install a material with lower efficiency in the 15 cm  $\times$  15 cm square central region to reduce neutron interactions and place higher efficiency material around it to effectively veto gammas coming through the CsI hole. We expect to use tungsten and quartz for this design.

### 2.2.3 Detector inefficiency

Inefficiency of photon veto counters arises when a photon interacts with the counter material, and the deposited energy is not observed. When photons have energies less than 150 MeV, the secondary products of photonuclear interactions are only neutrons. These neutrons do not leave their energies in a detector and escape from detection. Another source of the detection inefficiency is due to the punch-through photons which penetrate detectors without generating electromagnetic showers. This effect is prominent when gammas have energies less than 100 MeV. The third source of inefficiency, which is called the sampling effect, occurs when the incident gamma has energy less than 30 MeV. The lead absorbs all electrons in electromagnetic showers, and no signal reaches the plastic scintillator.

Figure 2.2 shows the photon detection inefficiency as a function of energy in lead-scintillator detectors [7]. Based on this figure, we assumed detector inefficiencies as shown in Table 2.1 for our simulation.

Energy Low-High (GeV)	MA/PV Inefficiency	CsI-Mid/Out Inefficiency	CsI-In/BA-Out Inefficiency	BA-In Inefficiency
0.0 - 0.02	$2 \times 10^{-1}$	1	1	1
0.02 - 0.04	$3 \times 10^{-2}$	$1 \times 10^{-1}$	1	1
0.04 - 0.06	$3 \times 10^{-3}$	$1 \times 10^{-2}$	1	1
0.06 - 0.10	$7 \times 10^{-4}$	$1 \times 10^{-3}$	$1 \times 10^{-2}$	1
0.10 - 0.20	$4 \times 10^{-4}$	$4 \times 10^{-4}$	$1 \times 10^{-3}$	1
0.20 - 0.40	$1 \times 10^{-4}$	$1 \times 10^{-4}$	$1 \times 10^{-4}$	1
0.40 - 1.00	$3 \times 10^{-5}$	$3 \times 10^{-5}$	$3 \times 10^{-5}$	1
1.00 - 3.00	$3 \times 10^{-6}$	$3 \times 10^{-6}$	$3 \times 10^{-6}$	$1 \times 10^{-1}$
3.00 - 10.0	$1 \times 10^{-6}$	$1 \times 10^{-6}$	$1 \times 10^{-6}$	$1 \times 10^{-2}$
10.0 - Inf.	$1 \times 10^{-6}$	$1 \times 10^{-6}$	$1 \times 10^{-6}$	$1 \times 10^{-3}$

Table 2.1: Detector inefficiencies used for background studies of  $K_L \rightarrow 2\pi^0$  decays. Each notation is defined as MA = Mask Anti, PV = Photon Veto, and BA = Back Anti. The BA-In is the 15 cm  $\times$  15 cm square central region of BA, surrounded by the BA-Out region which is set to have infinite area. The CsI calorimeter is categorized into three sections. 15 cm  $\times$  15 cm beam hole is surrounded by the 60 cm  $\times$  60 cm CsI-In region, which is inside the 120 cm  $\times$  120 cm CsI-Mid region. Outmost part is defined as the CsI-Out region which has 190  $\times$  190 cm<sup>2</sup>.

## 2.3 Event Weighting Technique

Since it takes excessive CPU resource to generate a number of background events and discard most of them by enabling photon veto counters, we used an event weighting technique as described below.

We first assumed that the veto counters are 100 % inefficient and kept each decay product. Thus, we can accumulate enough number of background events to reduce statistical errors. For each event, we then calculated a product of inefficiencies of each detector hit by photons, according to the inefficiency shown in Table 2.1 and assigned it as its event weight. Consequently the sum of these event weights represent the number of background events with active photon veto counters.

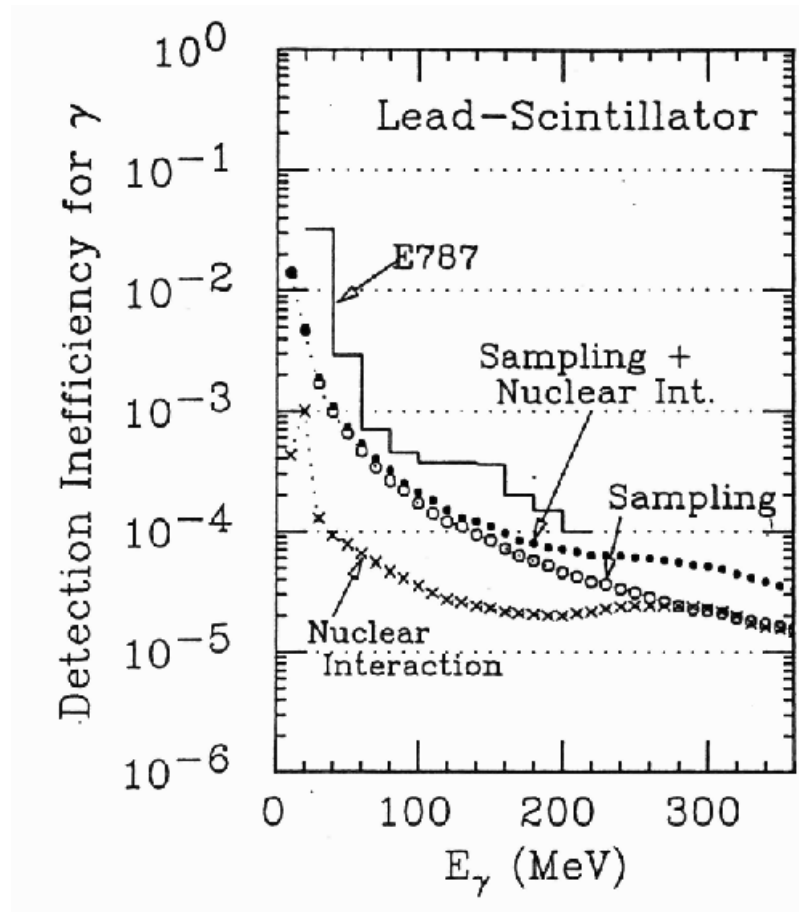


Figure 2.2: Photon detection inefficiency as a function of energy in lead-scintillator detectors quoted from Ref. [7]. The open circles, the cross points, and the dot points show the inefficiency due to the sampling effect, the photonuclear interaction, and their sum, respectively.

# Chapter 3

## Analysis without Time of Flight

Since the only available observable parameters for detecting the  $K_L \rightarrow \pi^0 \nu \bar{\nu}$  decay are the deposited energy and hit position of two gammas on the CsI calorimeter, it is crucial to veto extra gammas from other decay modes as effectively as possible. In addition,  $\pi^0$  from  $K_L \rightarrow \pi^0 \nu \bar{\nu}$  has the maximum momentum of 231 MeV/c, which is higher than other decay modes. Therefore, we can cut on the transverse momentum ( $p_t$ ) of  $\pi^0$ , relative to the beam axis, to reduce background events further. In this chapter, we look at the contribution of each of the background decay modes and study how to reject them without using time of flight.

### 3.1 Background Decay Modes

The secondary beam produced in beryllium target contains neutral particles such as  $K_L$ ,  $K_S$ ,  $\Lambda$ ,  $\Xi$ , and neutron. The decay products of these particles may contain one or multiple  $\pi^0$ 's, which can be misidentified as those coming from  $K_L \rightarrow \pi^0 \nu \bar{\nu}$  decays. This section describes possible background sources from such decays.

#### 3.1.1 $K_L \rightarrow \pi^0 \pi^0$

The most dominant background for the detection of  $K_L \rightarrow \pi^0 \nu \bar{\nu}$  is  $K_L \rightarrow \pi^0 \pi^0$ . While the branching ratio for  $K_L \rightarrow \pi^0 \pi^0$  decay is relatively low at  $9.36 \times 10^{-4}$ , much less than other background decay modes, the contribution from this decay mode is most dominant. This is because a  $K_L \rightarrow \pi^0 \pi^0$  event can fake a signal if only two photons out of four escape detection due to a detector inefficiency or overlapping on another photon cluster on the CsI calorimeter. Furthermore, when we reconstruct the  $\pi^0$  momentum from the energies of the two gamma clusters, since the maximum momentum of  $\pi^0$  transverse to the beam direction can be as high as 209 MeV/c, the distribution of  $\pi^0$  momentum of this mode looks very similar to that of  $K_L \rightarrow \pi^0 \nu \bar{\nu}$ . The later sections describe various methods to reduce  $K_L \rightarrow \pi^0 \pi^0$  background.

### 3.1.2 $K_L \rightarrow \pi^0\pi^0\pi^0$

Although  $K_L \rightarrow \pi^0\pi^0\pi^0$  has 300 times larger branching ratio than  $K_L \rightarrow \pi^0\pi^0$ , its reduction is much easier for two reasons. First, the probability of missing 4 photons is much smaller than that of missing 2 photons. Second, pions from this decay have less energies than  $K_L \rightarrow \pi^0\nu\bar{\nu}$  and  $K_L \rightarrow \pi^0\pi^0$  since the phase space of the three-pion final state is smaller than that of the two-pion final state. The transverse momentum of  $\pi^0$ 's produced in  $K_L \rightarrow \pi^0\pi^0\pi^0$  is less than 139 MeV/c, much smaller than those for  $K_L \rightarrow \pi^0\nu\bar{\nu}$  or  $K_L \rightarrow \pi^0\pi^0$ .

### 3.1.3 $\Lambda \rightarrow n\pi^0$

Even though  $\Lambda \rightarrow n\pi^0$  also has a large branching ratio (36%), because of  $\Lambda$ 's short life time ( $2.63 \times 10^{-10}$  s), the contribution from this decay is minor when we reject gammas from upstream by placing the Mask Anti. Also, this background can be easily reduced because the  $p_t$  of  $\pi^0$  from this decay is less than 104 MeV/c.

### 3.1.4 $K_L \rightarrow \gamma\gamma$

Requirement on  $p_t$  of two photons hit on the calorimeter can make the contribution from  $K_L \rightarrow \gamma\gamma$  negligible because two gammas from this decay has a transverse momentum of 0.

### 3.1.5 $nA \rightarrow \pi^0A$

It is highly possible that neutrons in the beam interact with material in the decay region and generate  $\pi^0$ 's, which might fake as if they were from  $K_L \rightarrow \pi^0\nu\bar{\nu}$ . To suppress this background, we must evacuate the decay volume at the level of  $3 \times 10^{-7}$  torr.

## 3.2 Event Selection

The following sections describe how we can reduce the number of background events by imposing each cut.

### 3.2.1 Clustering

The first step to reduce background events is requiring only two gamma hits on the CsI calorimeter. A cluster on the calorimeter is defined as a group of CsI blocks absorbing in-coming gamma energy. Sometimes photon detection inefficiency and cluster overlapping reduce the number of photon clusters to be two, and such events mimic as if they were coming from  $K_L \rightarrow \pi^0\nu\bar{\nu}$ .

The energy deposit of a photon in a crystal causes an electromagnetic shower which may reach the neighboring blocks. When two photons are close to each other on the calorimeter, the overlap of energy deposit forms a single cluster. This fused cluster reduces the number of photon hits on the calorimeter and may increase the background events for multiple-gamma-producing decay modes, such as  $K_L \rightarrow \pi^0\pi^0$  and  $K_L \rightarrow \pi^0\pi^0\pi^0$ .

In the MC study, if the distance between two photons on the calorimeter is less than twice of the crystal size, they were regarded as a single “fused” cluster, as shown in Table 3.1.

Distance Low-High (cm)	CsI-In/Mid	CsI-Out
0.0 - 5.0	Fused	Fused
5.0 - 10	Separated	Fused
10. - Inf.	Separated	Separated

Table 3.1: The fusion separation criteria in the CsI calorimeter used for studying the MC simulation. The decision is based on the distance between two photons. CsI-In, Mid, and Out are the notations defined in Table 2.1.

Another case for missing a photon on the calorimeter is due to the inefficiency of the calorimeter. When a low energy photon penetrates the calorimeter, it leaves no shower in a calorimeter block. We assumed the calorimeter inefficiency as indicated in Table 2.1.

### 3.2.2 Photon Veto

The photon vetoes surrounding the decay volume are the most powerful tool to reduce backgrounds from  $K_L \rightarrow \pi^0\pi^0$  and  $K_L \rightarrow \pi^0\pi^0\pi^0$ . Instead of vetoing events, we accumulated the weighted number of events as explained in Section 2.3.

### 3.2.3 Beam Axis Component of the Decay Vertex of $\pi^0$

The  $K_L$  decay vertex, thus  $\pi^0$  decay vertex<sup>1</sup>, is determined by assuming that the two gamma clusters on the CsI calorimeter is originated from a  $\pi^0$ . Denoting the deposited energy  $E_i$ , where  $i$  indicates the  $i$  th cluster on the calorimeter, and distance between the clusters  $r$ , we can find the beam axis component of the decay vertex,  $z_{vtx}$ :

$$z_{CsI} - z_{vtx} = \frac{r}{m_\pi} \sqrt{E_1 E_2} \quad (3.1)$$

---

<sup>1</sup>Since  $\pi^0$  has a lifetime of  $8.4 \times 10^{-17}$  s, the decay vertex of  $K_L$  and  $\pi^0$  are regarded as identical.

where  $z_{CsI}$  denotes the distance between the target and the calorimeter, and  $m_\pi = 135$  MeV is the rest mass of  $\pi^0$ . Energy and position resolutions of CsI introduces a fluctuation in the calculated  $z_{vtx}$ .

The effect of this cut is shown in Fig. 3.1. The vertical axis indicates the number of events expected for one year if we assume  $10^{13}$   $K_L$  decays. The upmost decay region is set at the position of the Mask Anti to sharply define the decay volume and veto the background events coming from upstream. The decay region ends at 171 m downstream of the target, or 15 m upstream of the calorimeter, to reduce background events coming from  $K_L \rightarrow \pi^0 \pi^0 \pi^0$ . 57.6 % of  $K_L \rightarrow \pi^0 \nu \bar{\nu}$  events survive this cut.

### 3.2.4 Transverse Momentum of $\pi^0$

$K_L \rightarrow \pi^0 \nu \bar{\nu}$  can have higher  $\pi^0$  momentum in the  $K_L$  CMS than other decay modes. This fact enables us to distinguish signal and background events by using  $p_t$  cut as mentioned in the beginning of this chapter. Figure 3.2 shows the  $p_t$  distributions of signal and background events. The  $p_t$  was required to be higher than 150 MeV/c to reduce backgrounds, while keeping 54 % of signal events.

### 3.2.5 Total Energy of Gamma Clusters on the CsI Calorimeter

By requiring the total energy deposit ( $E_t$ ) on the calorimeter to be within 5 GeV and 20 GeV, we can reduce background events such as  $\Lambda \rightarrow n \pi^0$  and  $K_L \rightarrow \pi^0 \pi^0 \pi^0$ . Figure 3.3 shows the distribution of  $E_t$  for each decay mode. We sacrifice 7.8 % of signal events for this cut.

Table 3.2 summarizes the above cuts.

The number of clusters on CsI	2
The beam axis component of the decay vertex ( $z_{vtx}$ )	$152m < z_{vtx} < 171m$
Pion momentum transverse to the beam axis ( $p_t$ )	$p_t > 150$ MeV
Total energy of two gamma clusters on CsI ( $E_t$ )	$5$ GeV $< E_t < 20$ GeV

Table 3.2: Cuts used in the MC simulation

## 3.3 The Number of $K_L \rightarrow \pi^0 \nu \bar{\nu}$ and Background Events

Figure 3.4 shows the  $p_t$  and  $z$  distribution of  $K_L \rightarrow \pi^0 \nu \bar{\nu}$  and various background decay modes after all the cuts except for  $z_{vtx}$  and  $p_t$  cuts have been made.

The number of  $K_L \rightarrow \pi^0 \nu \bar{\nu}$  events expected for a year is determined as,

$$\left( \begin{array}{c} \text{Number of} \\ K_L \rightarrow \pi^0 \nu \bar{\nu} \text{ events} \\ \text{expected for 1 year} \end{array} \right) = \left( \begin{array}{c} \text{Number of } K_L \text{ events} \\ \text{expected for one year} \end{array} \right) \times BR(K_L \rightarrow \pi^0 \nu \bar{\nu}) \times Acc(K_L \rightarrow \pi^0 \nu \bar{\nu}), \quad (3.2)$$

where  $BR$  is the predicted branching ratio of  $K_L \rightarrow \pi^0 \nu \bar{\nu}$  ( $3.0 \times 10^{-11}$ ), and  $Acc$  is the acceptance of  $K_L \rightarrow \pi^0 \nu \bar{\nu}$ . In this MC,  $10^5$   $K_L$  decays were generated, and we observed 6160 events after all the cuts have been made. Thus, substituting 0.0616 for  $Acc$  and setting number of  $K_L$  decays to be  $1 \times 10^{13}$  for a year, we can obtain the number of  $K_L \rightarrow \pi^0 \nu \bar{\nu}$  decays to be 18.5 (Fig. 3.5).

In the similar manner, we can obtain the number of  $K_L \rightarrow \pi^0 \pi^0$  and  $K_L \rightarrow \pi^0 \pi^0 \pi^0$  events for one year to be 5.0 and  $1.1 \times 10^{-4}$ , respectively.

High rise in the plots of  $K_L \rightarrow \pi^0 \pi^0$  and  $K_L \rightarrow \pi^0 \pi^0 \pi^0$  is the event which has three gamma hits on the calorimeter and one gamma hit on the detector with high inefficiency. The weight of such events creates a high rise of a histogram since they have several orders higher inefficiency than those events which have two photon hits on the veto counter. The number of events passed the Table 3.2 cuts are obtained from  $1 \times 10^5$   $K_L$  decays generated in MC. Increasing the generated number of events, we may observe more such events.

## Z<sub>vertex</sub>

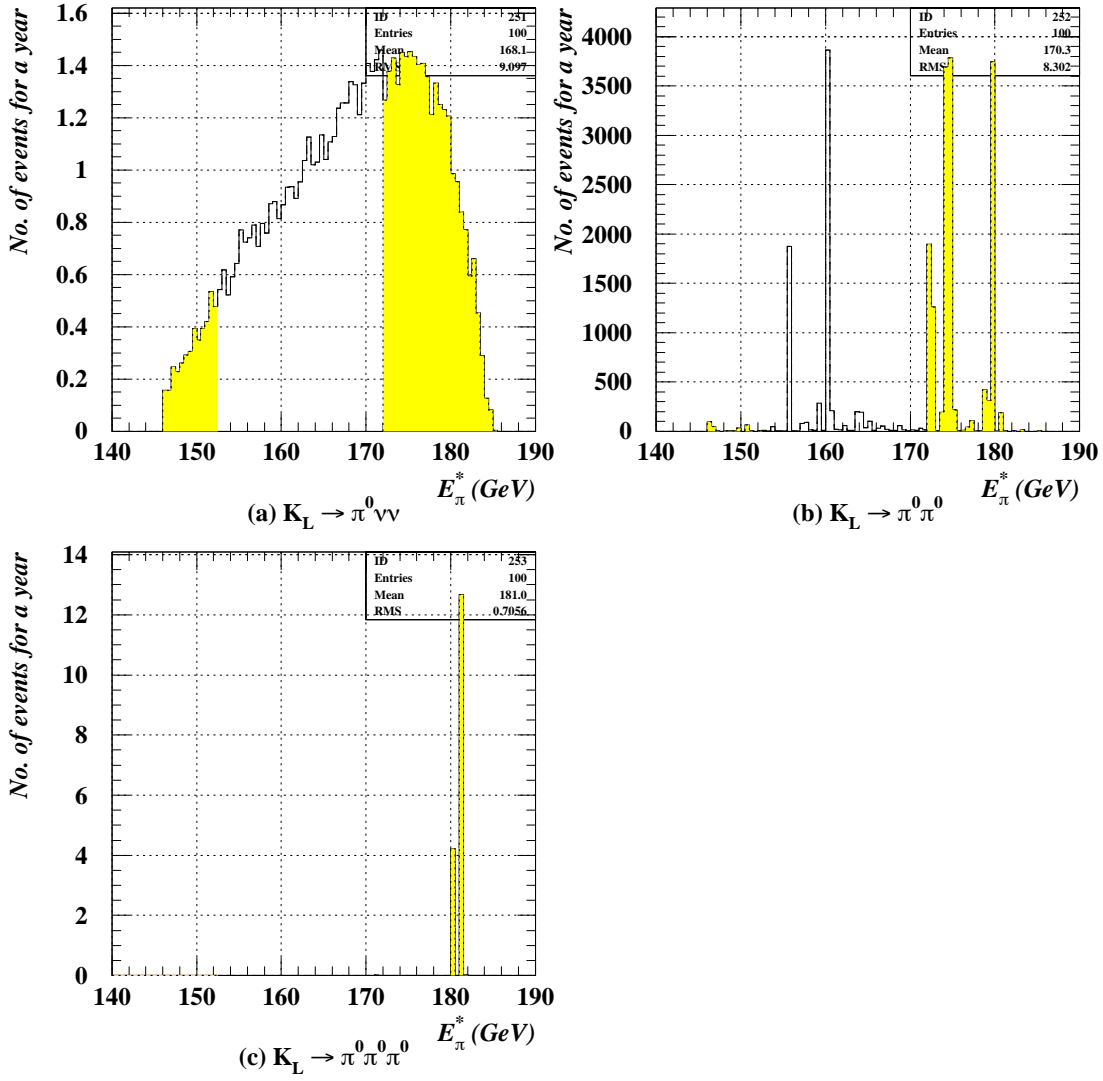


Figure 3.1: The beam axis component of the decay vertex of  $\pi^0$  for (a)  $K_L \rightarrow \pi^0 \nu \bar{\nu}$ , (b)  $K_L \rightarrow \pi^0 \pi^0$ , and (c)  $K_L \rightarrow \pi^0 \pi^0 \pi^0$ . The shaded area is discarded by the condition,  $152 < z_{vtx} < 171$  m.

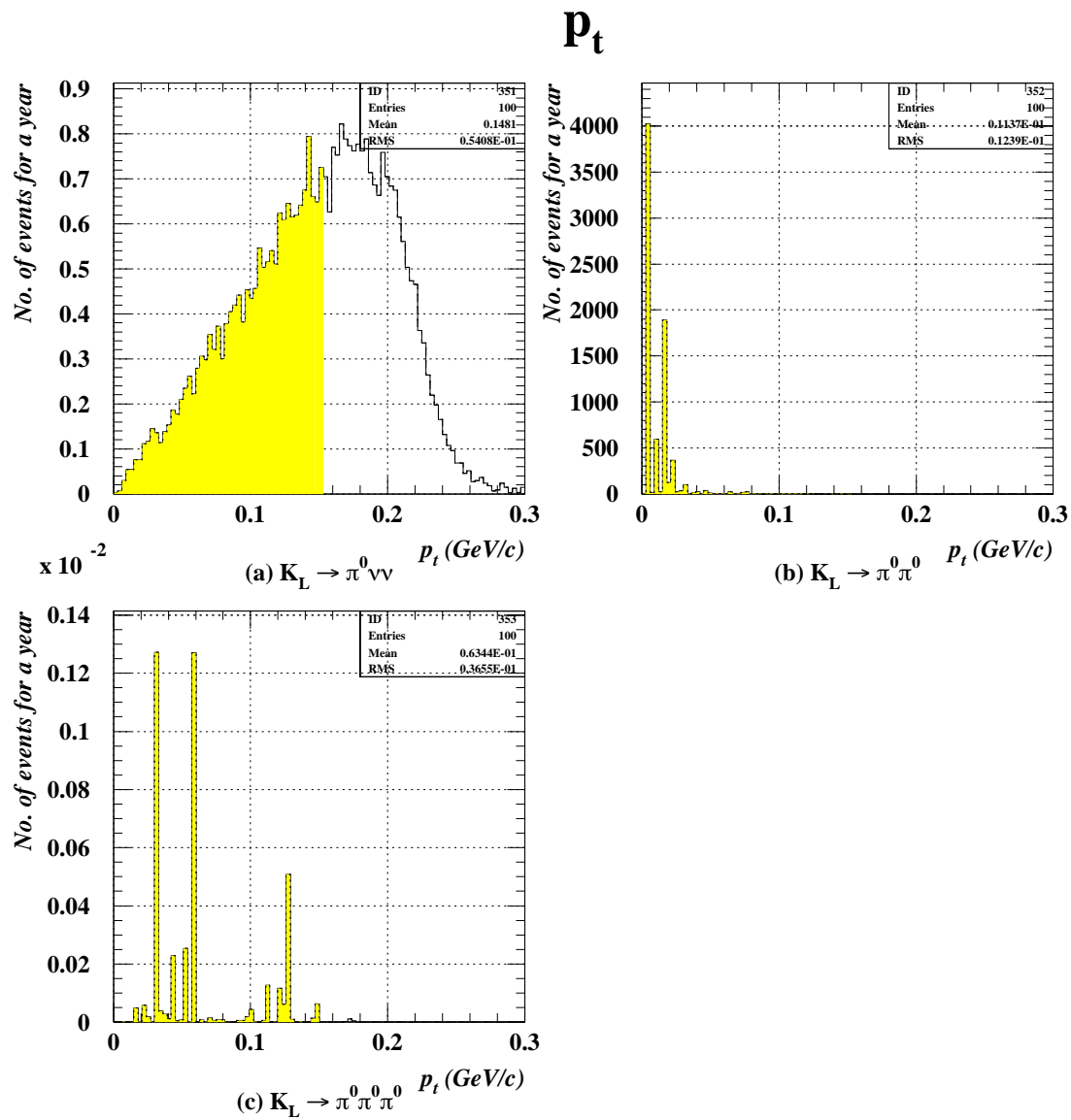


Figure 3.2: The transverse momentum distribution for (a)  $K_L \rightarrow \pi^0 \nu \bar{\nu}$ , (b)  $K_L \rightarrow \pi^0 \pi^0$ , and (c)  $K_L \rightarrow \pi^0 \pi^0 \pi^0$ . The shaded area is discarded by the condition,  $p_t > 150$  MeV.

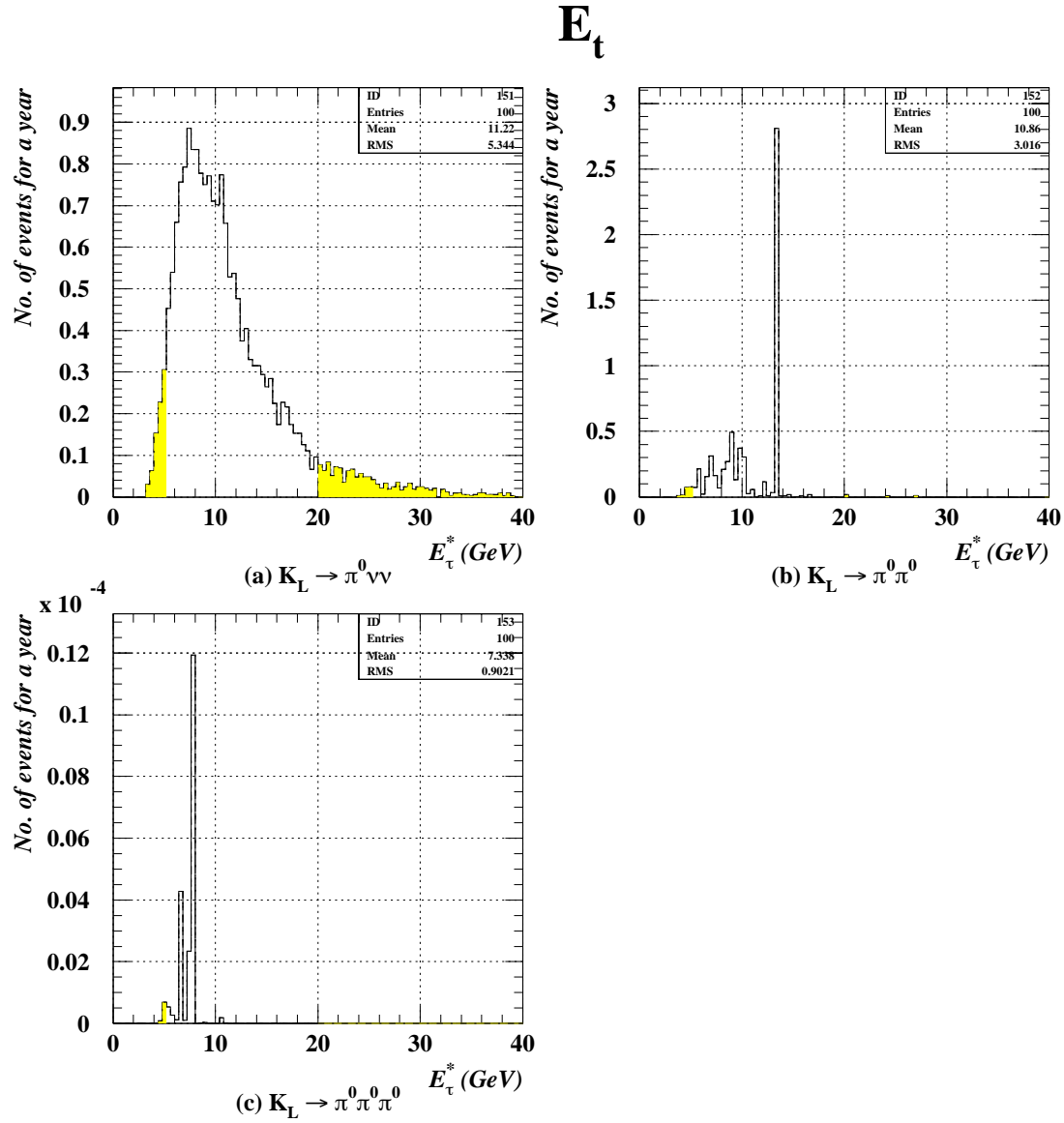


Figure 3.3: The total energy deposit in the CsI clusters for (a)  $K_L \rightarrow \pi^0 \nu \bar{\nu}$ , (b)  $K_L \rightarrow \pi^0 \pi^0$ , and (c)  $K_L \rightarrow \pi^0 \pi^0 \pi^0$ . The shaded area is discarded by the condition,  $E_t > 5$  GeV.

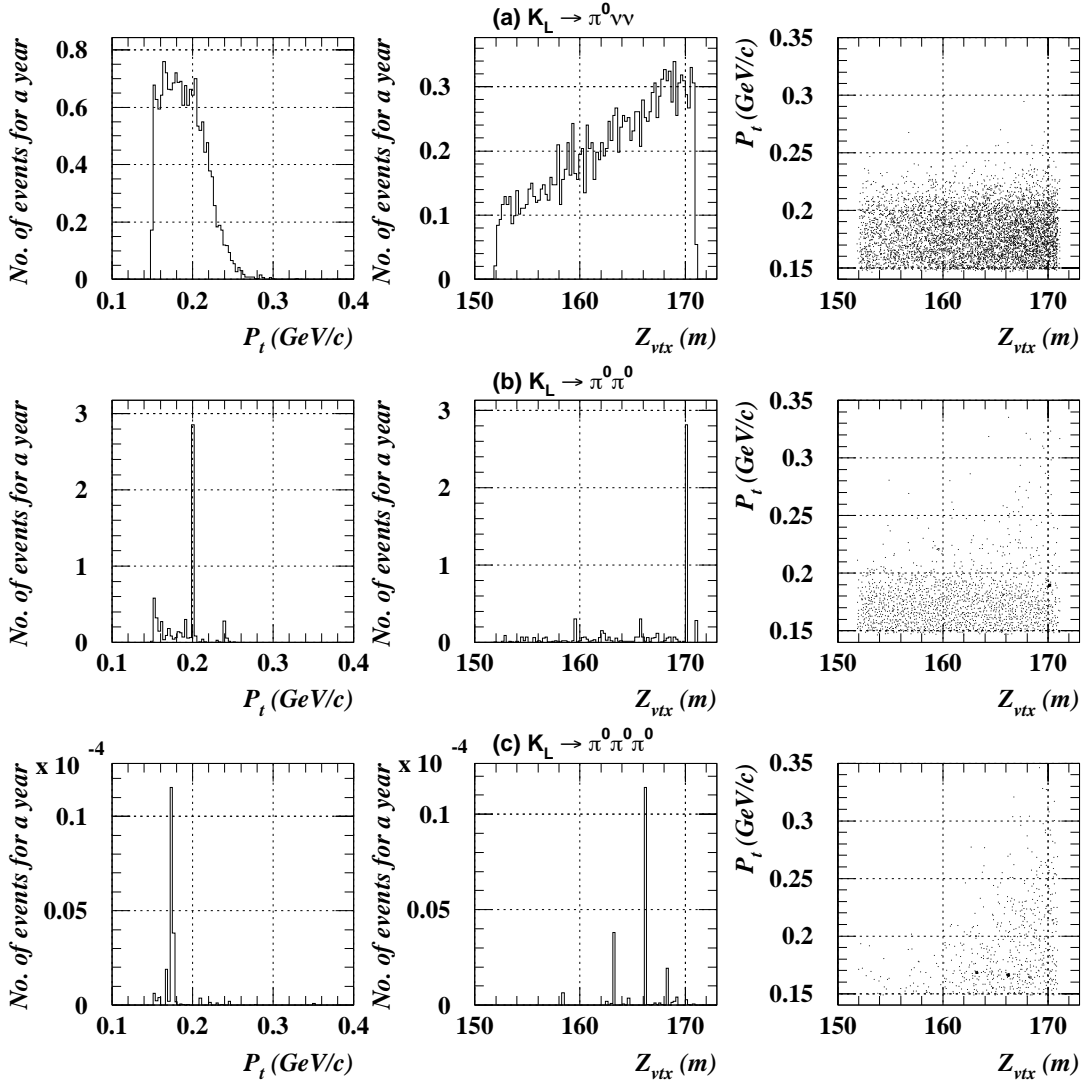


Figure 3.4: The z vertex and  $P_t$  distributions for (a)  $K_L \rightarrow \pi^0 \nu \bar{\nu}$  (b)  $K_L \rightarrow \pi^0 \pi^0$ , and (c)  $K_L \rightarrow \pi^0 \pi^0 \pi^0$  events from a Monte Carlo simulation

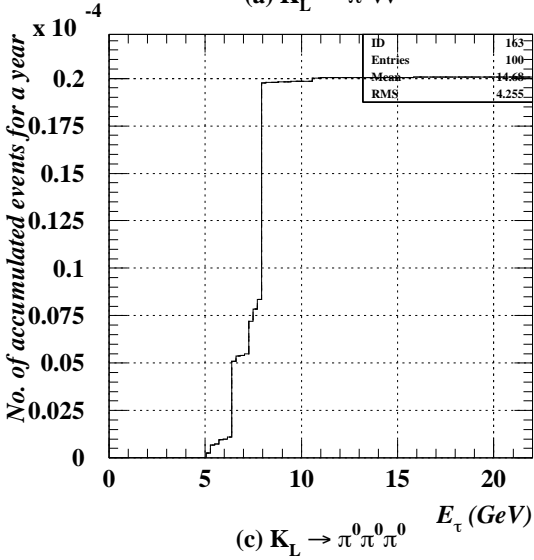
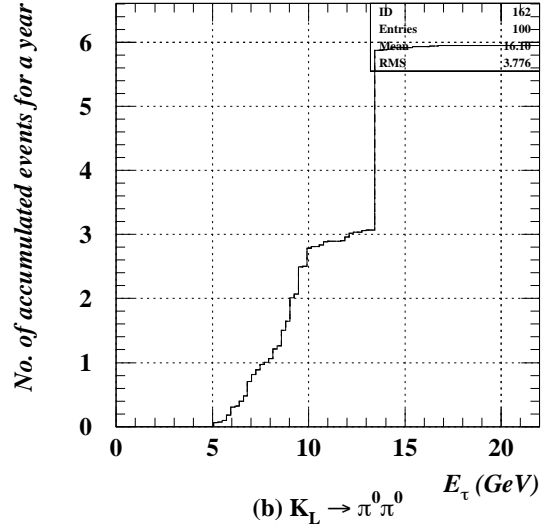
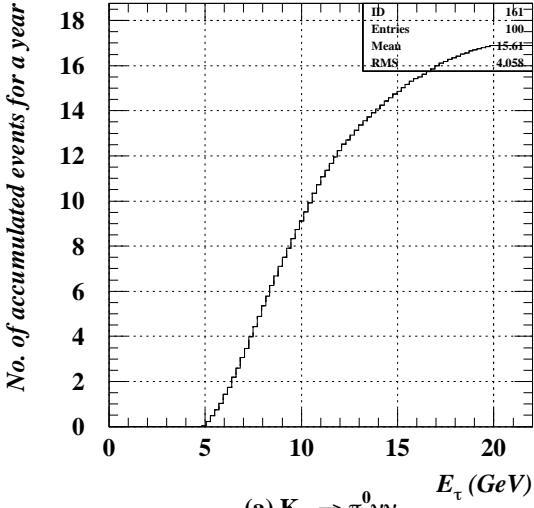


Figure 3.5: The integrated number of events expected for one year operation after all cuts in Table 3.2 had been made is shown for (a)  $K_L \rightarrow \pi^0 \nu \bar{\nu}$ , (b)  $K_L \rightarrow \pi^0 \pi^0$ , and (c)  $K_L \rightarrow \pi^0 \pi^0 \pi^0$  at  $E_t = 20$  GeV.

# Chapter 4

## Time of Flight Measurement

In the center of mass system of kaons, there is a striking difference in  $\pi^0$  energy ( $E_\pi^*$ ) distribution between the signal decay mode,  $K_L \rightarrow \pi^0 \nu \bar{\nu}$ , and the most dominant background mode,  $K_L \rightarrow \pi^0 \pi^0$ , as shown in Fig. 4.1. Because the  $K_L \rightarrow \pi^0 \nu \bar{\nu}$  decay is a 3-body decay,  $\pi^0$  has an extended  $E_\pi^*$  distribution, whereas  $K_L \rightarrow \pi^0 \pi^0$  has a sharp peak at  $E_\pi^*=249$  MeV because it is a 2-body decay. This difference motivates us to reduce the relative number of  $K_L \rightarrow \pi^0 \pi^0$  by imposing a cut on  $E_\pi^*$ . By measuring the time of flight of  $K_L$ , we can measure the  $\beta$  of  $K_L$  and Lorentz-transform the pion energy from the laboratory frame to the CMS of  $K_L$ . However, we must keep in mind that Fig. 4.1 has no smearing effect; in the actual experiment, energy and time resolution of the calorimeter smears the distribution, and with insufficient resolution, the two plots may be indistinguishable.

Here, in this chapter, we will first see a kinematic method for utilizing the time of flight measurement to use the pion energy cut. We will then compare different conditions to study the feasibility of time of flight.

### 4.1 Kinematics and Method

First, let us take a look at how we can Lorentz-transform pion energy and momentum from the laboratory frame to the center of mass system of  $K_L$  to obtain the distributions shown in Fig. 4.1

For the calculation of the pion energy in the CMS of a kaon, we need two parameters, namely, pion energy in the laboratory frame,  $E_\pi$ , and the  $\beta$  of  $K_L$ .

$$E_\pi^* = \beta E_\pi - \gamma \beta p_\pi \tag{4.1}$$

where  $\gamma$  is defined as

$$\gamma = \frac{1}{\sqrt{1 - \beta^2}}. \tag{4.2}$$

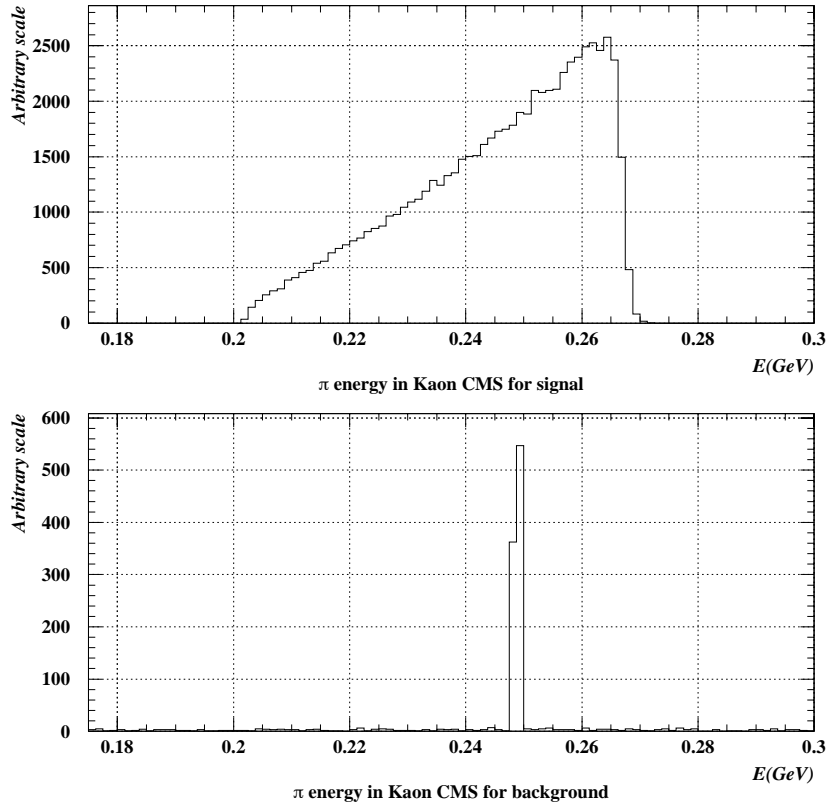


Figure 4.1:  $E_\pi^*$  distribution with no smearing. The above figure shows the extended distribution of  $\pi^0$  coming from  $K_L \rightarrow \pi^0 \nu \bar{\nu}$  while the bottom one indicates the sharp peak of  $\pi^0$  from  $K_L \rightarrow \pi^0 \pi^0$ . The small histograms in the  $K_L \rightarrow \pi^0 \pi^0$  figure are due to gammas coming from different  $\pi^0$ 's.

The time of flight between the target and the calorimeter,  $T_{of}$ , is related to  $\beta$  as,

$$T_{of} = \frac{z_{vtx}}{c\beta} + \frac{z_{CsI} - z_{vtx}}{c}, \quad (4.3)$$

where  $z_{CsI}$  is the position of the CsI calorimeter, and  $z_{vtx}$  is the decay vertex position in  $z$ . The  $\beta$  is obtained by the equation

$$\beta = \frac{z_{vtx}}{c(T_{of} - \frac{z_{CsI} - z_{vtx}}{c})}. \quad (4.4)$$

Thus, parameters  $z_{vtx}$  and  $T_{of}$  enable us to obtain pion energy in the CMS of kaon.

By tightly bunching the proton beam, we can measure  $T_{of}$  as the difference between the time protons hit the target and the time  $\gamma$ 's hit CsI.

## 4.2 Time and Energy resolutions

Now, let us take time and energy resolutions into consideration. In the Monte Carlo study, the  $T_{of}$  and cluster energies were smeared by the time resolution and energy resolution,  $\sigma_T$  and  $\sigma_E$ , respectively, with Gaussian distribution. A typical CsI block used in the KTeV experiment can produce 10 photo-electrons per MeV, giving a resolution of

$$\sigma_E \equiv \frac{\delta E}{E} = 0.0045 + \frac{0.02}{\sqrt{E(GeV)}}, \quad (4.5)$$

as shown in Fig. 4.2. Time resolution for the KAMI spectrometer is still unknown. We set  $\sigma_T$  to be 500 ps, 400 ps, 300 ps, 200 ps, 100 ps, and 50 ps. Figure 4.3 and Fig. 4.4 show the  $E_\pi^*$  distribution for  $K_L \rightarrow \pi^0 \nu \bar{\nu}$  and  $K_L \rightarrow \pi^0 \pi^0$ , respectively, considering the time and energy resolution into account. In these plots, different lines stand for different cuts on the momentum of kaons,  $p_{K_L}$ .

With larger  $\sigma_T$ , it is not possible to make a distinction between these distributions. The full-width-at-half-maximum (FWHM) of both  $K_L \rightarrow \pi^0 \nu \bar{\nu}$  and  $K_L \rightarrow \pi^0 \pi^0$  distributions is identical for  $\sigma_T$  larger than 200 ps. Even with  $\sigma_T=50$  ps, the distribution of  $E_\pi^*$  for  $K_L \rightarrow \pi^0 \pi^0$  has a width of around 50 MeV/c without any constraints on the initial  $K_L$  momentum. Since the  $\gamma$ -factor increases rapidly near  $\beta \sim 1$ , the symmetric smearing of  $T_{of}$  causes a long tail on the higher  $E_\pi^*$  region.

## 4.3 Cut on the $\pi^0$ Energy in the $K_L$ Center of Mass System

After making cuts on  $E_t, p_t$ , and  $z_{vtx}$ , we now observe the effect of another cut on  $E_\pi^*$  in this section.

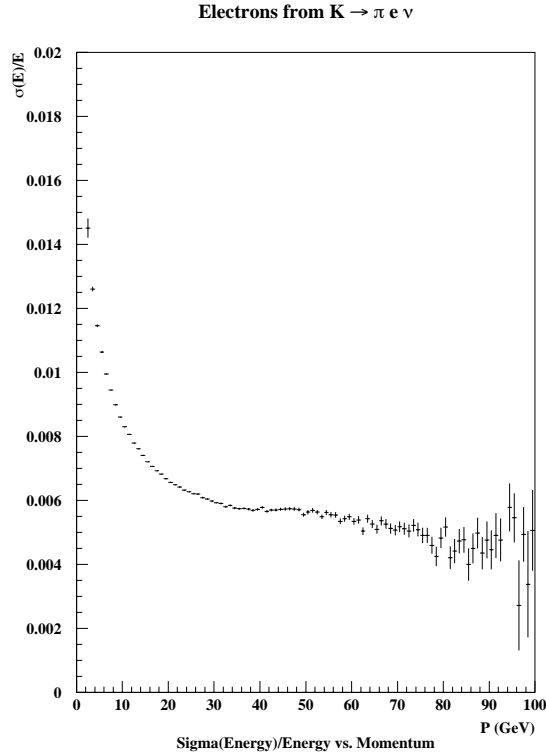


Figure 4.2: Energy resolution vs. momentum for electrons. The contribution from momentum resolution is removed [11].

### 4.3.1 $\beta$ Cut

When we perform a Lorentz-transformation of  $\pi^0$  energy from laboratory frame to the CMS of  $K_L$ , we must require that  $\beta$  of equation (4.4) should be less than 1. Figure 4.5 shows the distribution of reconstructed  $\beta$  for different time resolutions,  $\sigma_T$ . As can be seen, worse time resolution reduces the fraction of events with  $\beta < 1$ . Table 4.1 summarizes the fraction of events satisfying the  $\beta < 1$  cut. Because initial  $K_L$  of  $K_L \rightarrow \pi^0 \nu \bar{\nu}$  tends to have higher momentum than that of  $K_L \rightarrow \pi^0 \pi^0$ ,  $K_L \rightarrow \pi^0 \nu \bar{\nu}$  has smaller survival fraction.

$\sigma_T$ (ps)	$K_L \rightarrow \pi^0 \nu \bar{\nu}$	$K_L \rightarrow \pi^0 \pi^0$
500	67.8 %	81.1 %
400	70.7 %	85.4 %
300	75.7 %	89.4 %
200	82.3 %	94.7 %
100	91.2 %	99.1 %
50	97.2 %	99.7 %

Table 4.1: The ratio of events which passed the requirement  $\beta < 1$ .

### 4.3.2 The Number of Events Observed for a Year

Let us now look at the number of  $K_L \rightarrow \pi^0 \nu \bar{\nu}$  and  $K_L \rightarrow \pi^0 \pi^0$  events expected for one year. For this calculation, we use the equation 3.2 presented in Chapter 3, or again,

$$\left( \begin{array}{c} \text{Number of} \\ K_L \rightarrow \pi^0 \nu \bar{\nu} \text{ events} \\ \text{expected for 1 year} \end{array} \right) = \left( \begin{array}{c} \text{Number of } K_L \text{ decays} \\ \text{expected for 1 year} \\ (1 \times 10^{13}) \end{array} \right) \times BR(K_L \rightarrow \pi^0 \nu \bar{\nu}) \times Acc(K_L \rightarrow \pi^0 \nu \bar{\nu}),$$

$$\left( \begin{array}{c} \text{Number of} \\ K_L \rightarrow \pi^0 \pi^0 \text{ events} \\ \text{expected for 1 year} \end{array} \right) = \left( \begin{array}{c} \text{Number of } K_L \text{ decays} \\ \text{expected for 1 year} \\ (1 \times 10^{13}) \end{array} \right) \times BR(K_L \rightarrow \pi^0 \pi^0) \times Acc(K_L \rightarrow \pi^0 \pi^0).$$

Figures 4.6 and 4.7 show the calculated number of expected events vs.  $E_\pi^*$  cut. At each point of  $E_\pi^*$ , the corresponding vertical axis value shows the accumulated number of events expected for one year satisfying pion energy less than  $E_\pi^*$ . If  $\sigma_T = 50$  ps, for instance, we can expect to find about 10  $K_L \rightarrow \pi^0 \nu \bar{\nu}$  events when we select events satisfying  $E_\pi^* < 250$  MeV, using  $K_L$  beam of the momentum  $< 120$  GeV/c ( $< 50$  GeV/c). By inspecting the corresponding plot for  $K_L \rightarrow \pi^0 \pi^0$ , we can expect 1.5  $K_L \rightarrow \pi^0 \pi^0$  background events. As time resolution gets worse, the accumulated number of events decreases, as predicted from the  $\beta$  acceptance. When  $\sigma_T$  becomes larger, the number of background events increases at low  $E_\pi^*$ . By using low momentum  $K_L$ , we can reduce the background level, although we will sacrifice the number of signal events.

## 4.4 Results with Different Conditions

### 4.4.1 Energy Resolution

In order to find the effect of the energy resolution, we simply changed the values in the equation (4.5) to half:

$$\sigma_E \equiv \frac{\delta E}{E} = 0.00225 + \frac{0.01}{\sqrt{E}}. \quad (4.6)$$

The number of events expected for 1 year for different  $\sigma_T$  is shown in Figures 4.8 and 4.9.

Comparing Figures from 4.6 to 4.9, we can find little difference in the number of expected events for one year.

### 4.4.2 Gamma Veto Inefficiency

For another comparison, let us assume that the inefficiency for low energy photon gets worse than Table 2.1. Here we assume that we cannot detect photons with energy less than 20 MeV. In other words, inefficiency of the Vacuum Veto and Mask Anti was set to 1 for photon energy less than 20 MeV. The number of  $K_L \rightarrow \pi^0 \pi^0$  events almost triples as shown in Fig. 4.10. In case of  $\sigma_T=50$  ps,  $E_\pi^*$  cut at around 235 MeV, without vetoing gammas having energies less than 20 MeV, gives the equivalent number of background event as  $E_\pi^*$  cut at 250 MeV in the standard configuration.

$$\mathbf{K}_L \rightarrow \pi^0 \nu \bar{\nu}$$

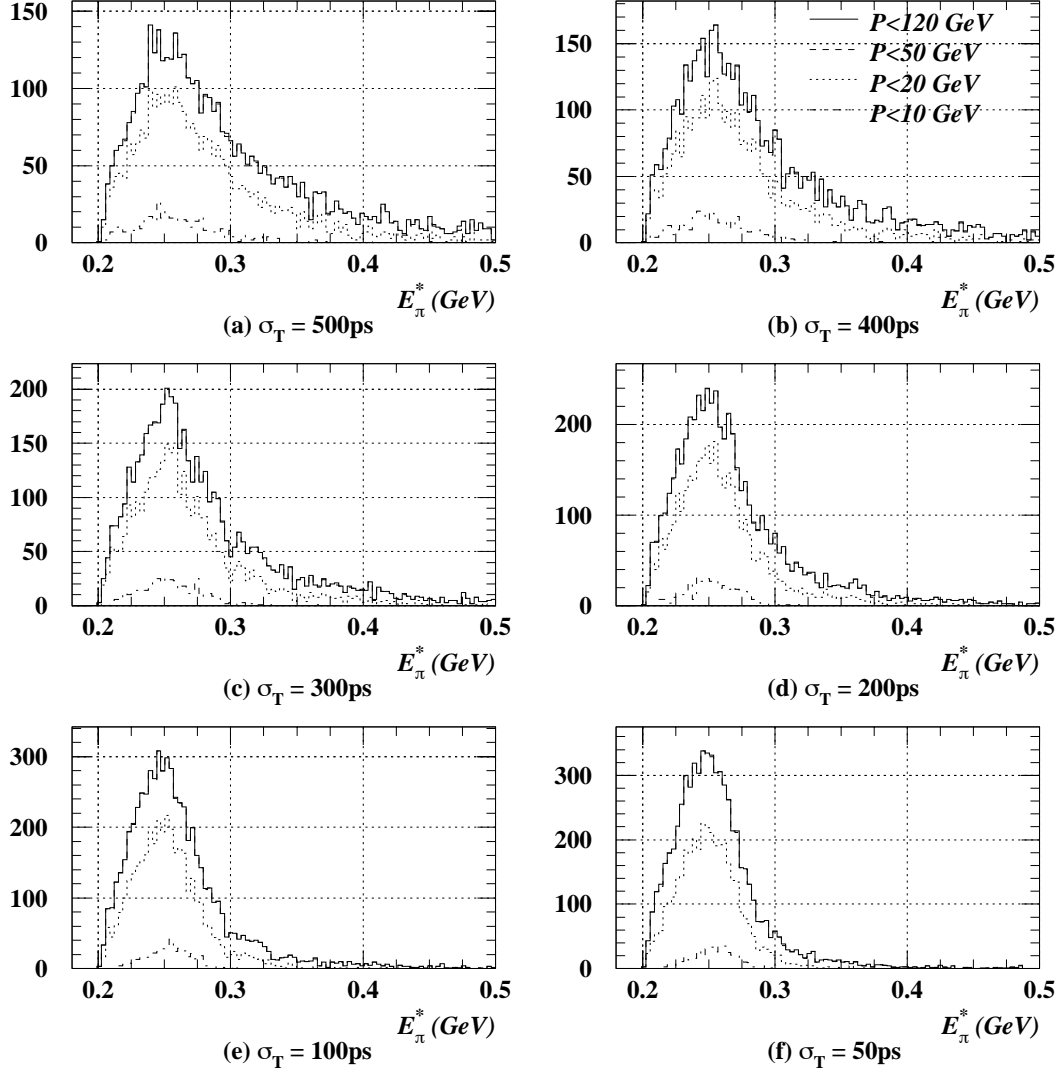


Figure 4.3:  $E_\pi^*$  distribution for  $K_L \rightarrow \pi^0 \nu \bar{\nu}$  with smearing effects. (a)  $\sigma_T = 500$  ps, (b)  $\sigma_T = 400$  ps, (c)  $\sigma_T = 300$  ps, (d)  $\sigma_T = 200$  ps, (e)  $\sigma_T = 100$  ps, and (f)  $\sigma_T = 50$  ps. The solid line represents the  $K_L$  momentum to be less than 120 GeV/c, while dashed line for 50 GeV/c, half-dotted line for 20 GeV/c, and dotted line for 10 GeV/c. Because the distribution of initial  $K_L$  momentum for survived events stretches from  $p_{K_L} = 5$  GeV to  $p_{K_L} = 50$  GeV for  $K_L \rightarrow \pi^0 \nu \bar{\nu}$  and from  $p_{K_L} = 5$  GeV to  $p_{K_L} = 30$  GeV for  $K_L \rightarrow \pi^0 \pi^0$ , there can be seen overlap of  $p_{K_L} < 120$  GeV and  $p_{K_L} < 50$  GeV plots for  $K_L \rightarrow \pi^0 \nu \bar{\nu}$  and  $p_{K_L} < 120$  GeV  $p_{K_L} < 50$  GeV, and  $p_{K_L} < 20$  GeV plots for  $K_L \rightarrow \pi^0 \pi^0$ .

$$\mathbf{K}_L \rightarrow \pi^0 \pi^0$$

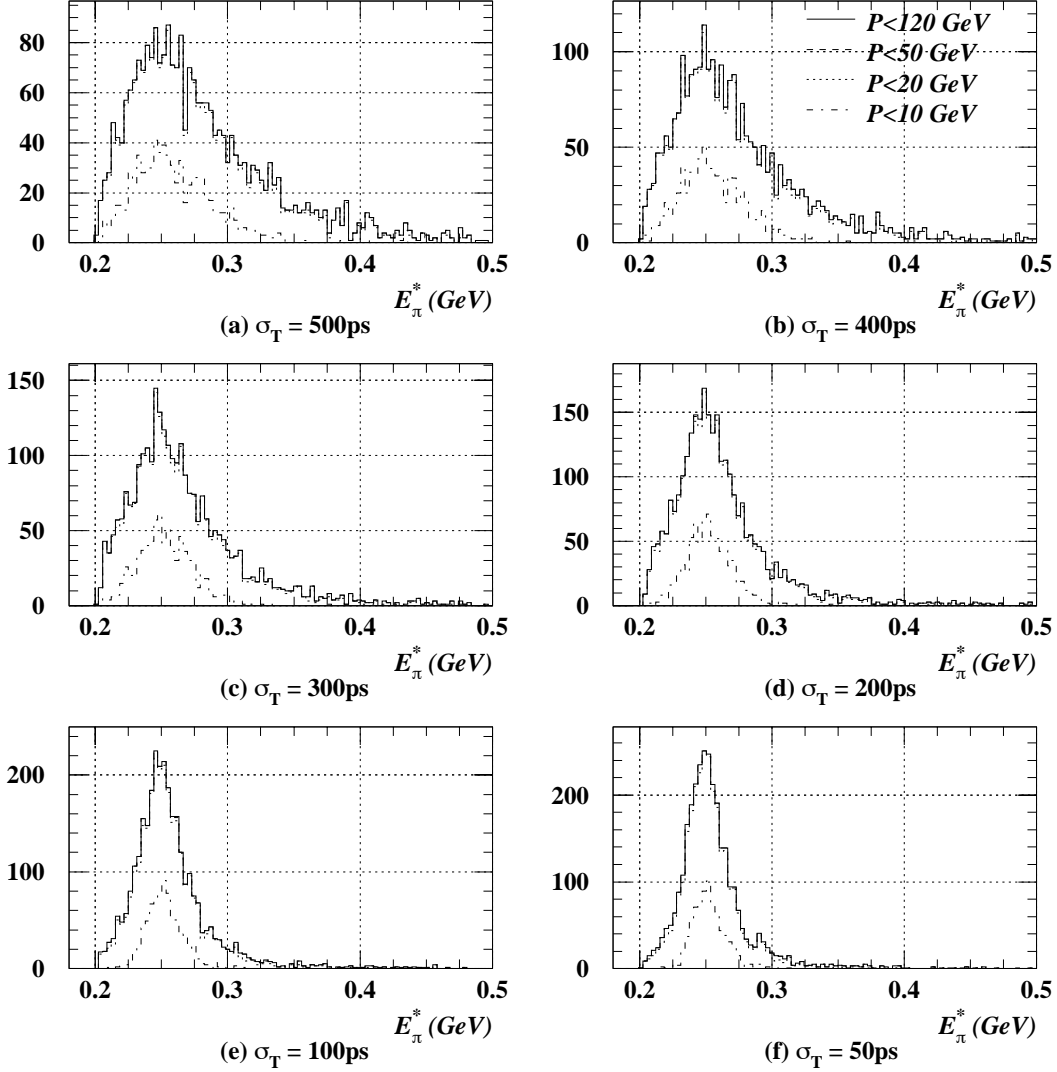


Figure 4.4:  $E_\pi^*$  distribution for  $K_L \rightarrow \pi^0 \pi^0$  with smearing effects. (a)  $\sigma_T = 500$  ps, (b)  $\sigma_T = 400$  ps, (c)  $\sigma_T = 300$  ps, (d)  $\sigma_T = 200$  ps, (e)  $\sigma_T = 100$  ps, and (f)  $\sigma_T = 50$  ps. The solid line represents the  $K_L$  momentum to be less than 120 GeV/c, while dashed line for 50 GeV/c, half-dotted line for 20 GeV/c, and dotted line for 10 GeV/c. Because the distribution of initial  $K_L$  momentum for survived events stretches from  $p_{K_L} = 5$  GeV to  $p_{K_L} = 50$  GeV for  $K_L \rightarrow \pi^0 \nu \bar{\nu}$  and from  $p_{K_L} = 5$  GeV to  $p_{K_L} = 30$  GeV for  $K_L \rightarrow \pi^0 \pi^0$ , there can be seen overlap of  $p_{K_L} < 120$  GeV and  $p_{K_L} < 50$  GeV plots for  $K_L \rightarrow \pi^0 \nu \bar{\nu}$  and  $p_{K_L} < 120$  GeV  $p_{K_L} < 50$  GeV, and  $p_{K_L} < 20$  GeV plots for  $K_L \rightarrow \pi^0 \pi^0$ .

$$\mathbf{K}_L \rightarrow \pi^0 \nu \nu$$

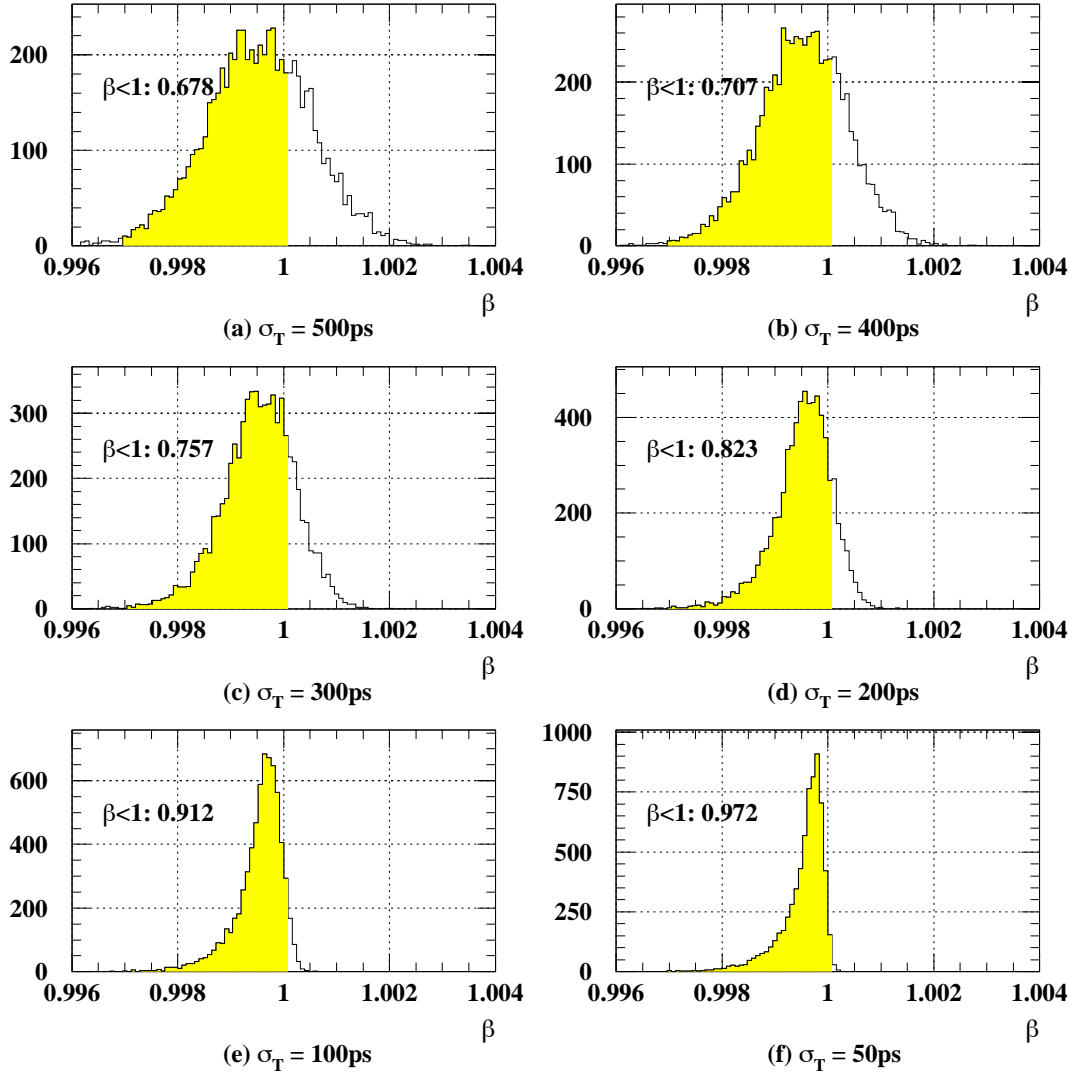


Figure 4.5: The distribution of calculated  $\beta$  is shown for different time resolutions,  $\sigma_T$ , to be (a)500 ps, (b)400 ps, (c)300 ps, (d)200 ps (e) 100 ps, and (f)50 ps. The shaded area shows  $\beta < 1$  region which is used for  $E_\pi^*$  calculation. The number within each plot shows the fraction of events satisfying  $\beta < 1$ .

$$K_L \rightarrow \pi^0 \nu \bar{\nu}$$

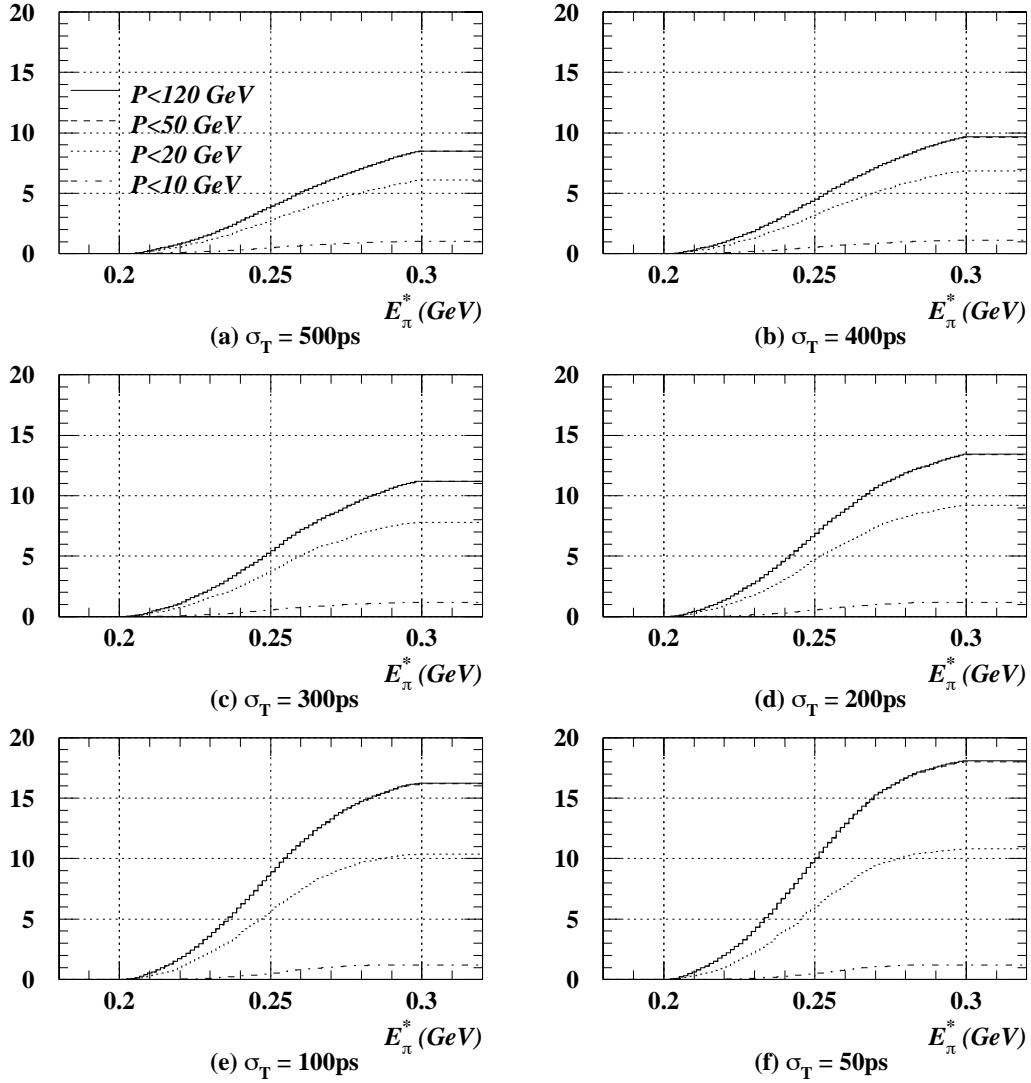


Figure 4.6: The number of events expected for  $K_L \rightarrow \pi^0 \nu \bar{\nu}$  for one year operation is shown as a function of the cut on  $E_\pi^*$ . (a)  $\sigma_T = 500$  ps, (b)  $\sigma_T = 400$  ps, (c)  $\sigma_T = 300$  ps, (d)  $\sigma_T = 200$  ps, (e)  $\sigma_T = 100$  ps, and (f)  $\sigma_T = 50$  ps. The solid line represents the  $K_L$  momentum to be less than 120 GeV/c, while dashed line for 50 GeV/c, half-dotted line for 20 GeV/c, and dotted line for 10 GeV/c.

$$\mathbf{K}_L \rightarrow \pi^0 \pi^0$$

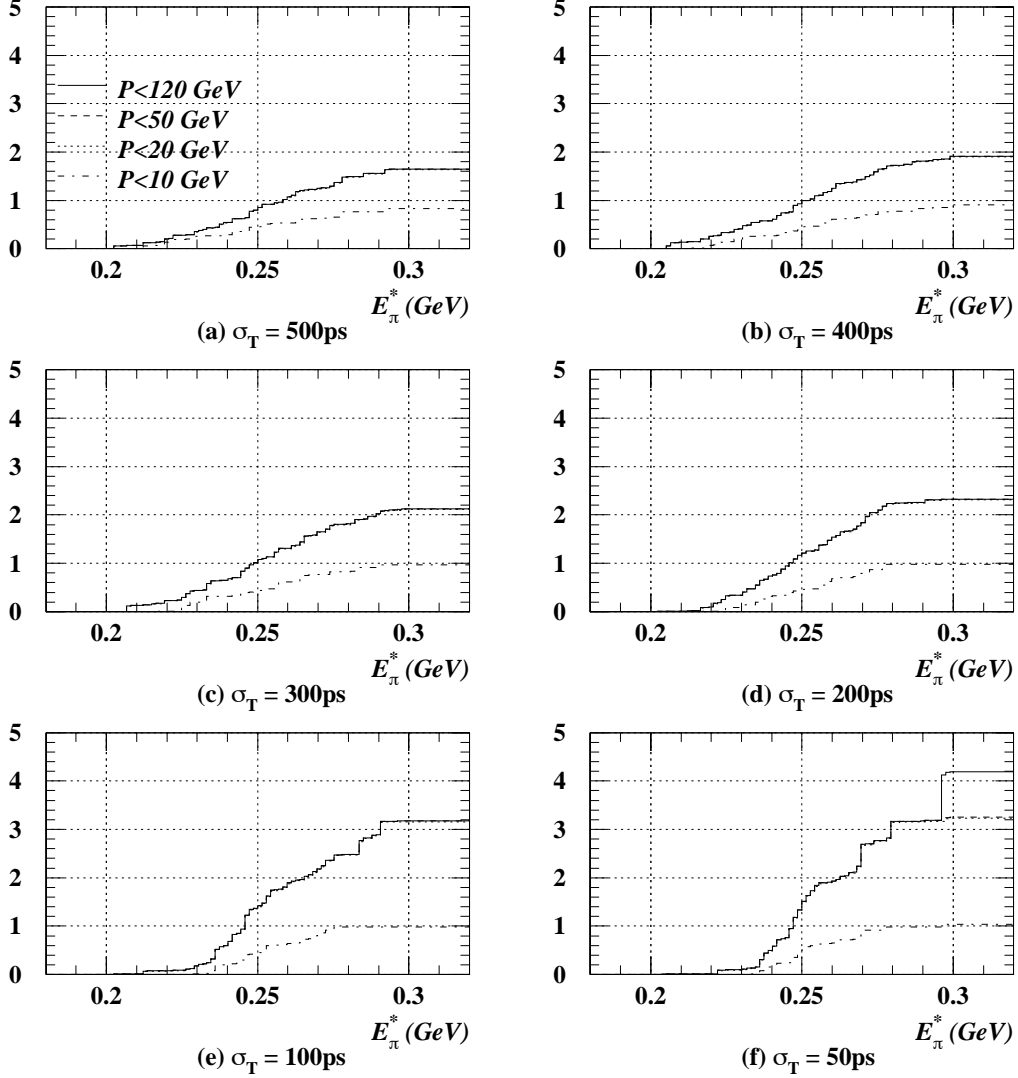


Figure 4.7: The number of events expected for  $K_L \rightarrow \pi^0 \pi^0$  for one year operation is shown as a function of the cut on  $E_\pi^*$ . (a)  $\sigma_T = 500$  ps, (b)  $\sigma_T = 400$  ps, (c)  $\sigma_T = 300$  ps, (d)  $\sigma_T = 200$  ps, (e)  $\sigma_T = 100$  ps, and (f)  $\sigma_T = 50$  ps. The solid line represents the  $K_L$  momentum to be less than 120 GeV/c, while dashed line for 50 GeV/c, half-dotted line for 20 GeV/c, and dotted line for 10 GeV/c.

$$\mathbf{K}_L \rightarrow \pi^0 \nu \bar{\nu}$$

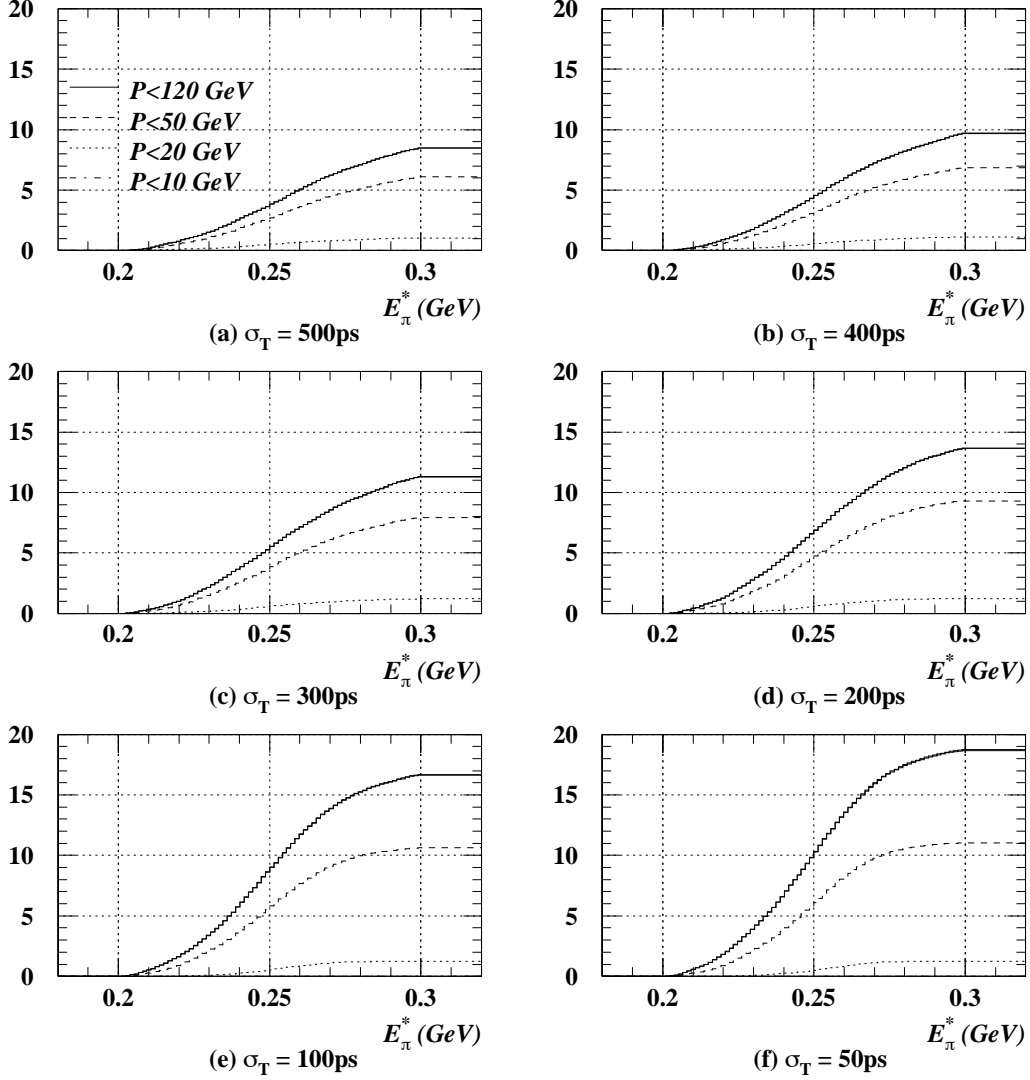


Figure 4.8: The number of events expected for  $K_L \rightarrow \pi^0 \nu \bar{\nu}$  for one year operation is shown as a function of the cut on  $E_\pi^*$ . A smaller  $\sigma_E$  in equation (4.6) is used here. (a)  $\sigma_T = 500$  ps, (b)  $\sigma_T = 400$  ps, (c)  $\sigma_T = 300$  ps, (d)  $\sigma_T = 200$  ps, (e)  $\sigma_T = 100$  ps, and (f)  $\sigma_T = 50$  ps. The solid line represents the  $K_L$  momentum to be less than 120 GeV/c, while dashed line for 50 GeV/c, half-dotted line for 20 GeV/c, and dotted line for 10 GeV/c.

$$\mathbf{K}_L \rightarrow \pi^0 \pi^0$$

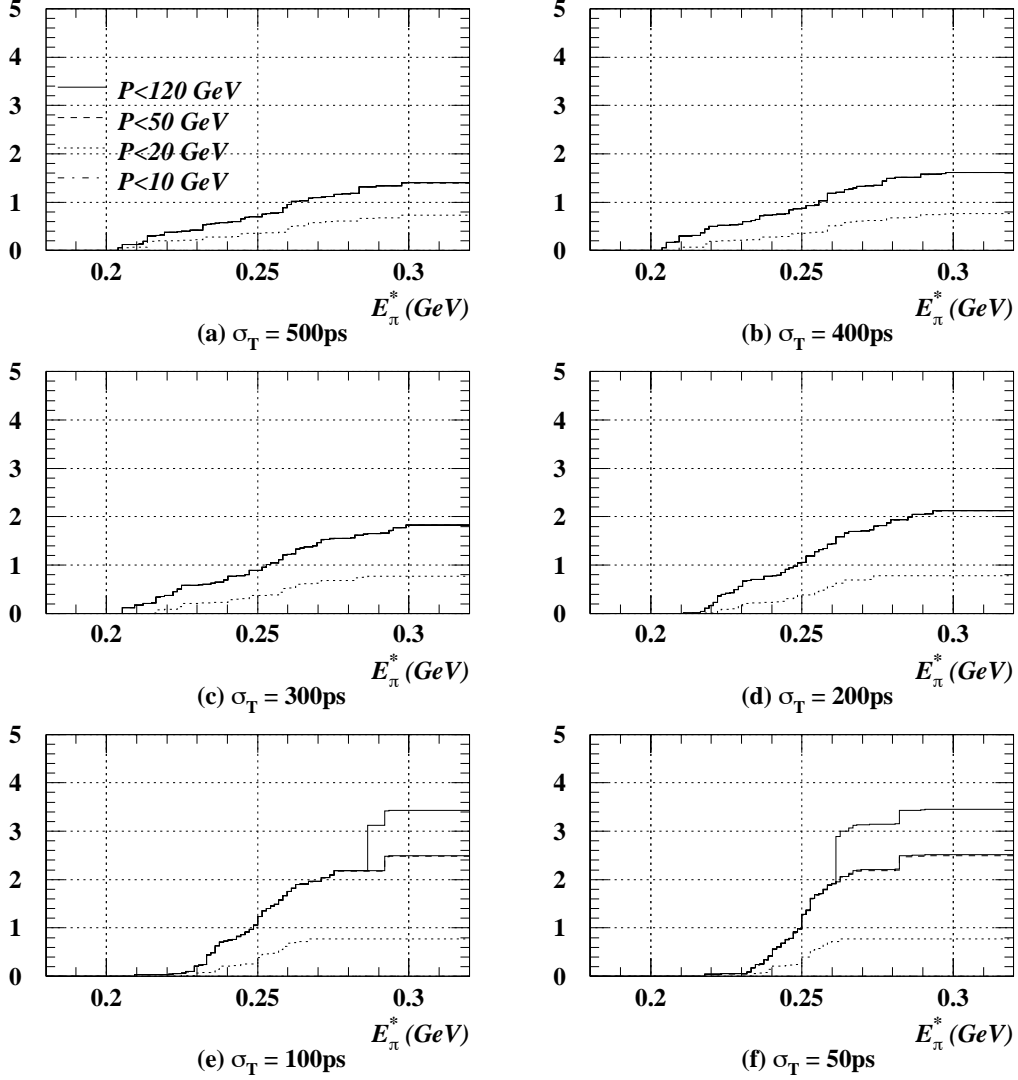


Figure 4.9: The number of events expected for  $K_L \rightarrow \pi^0 \pi^0$  for one year operation is shown as a function of the cut on  $E_\pi^*$ . A smaller  $\sigma_E$  in equation (4.6) is used here. (a)  $\sigma_T = 500$  ps, (b)  $\sigma_T = 400$  ps, (c)  $\sigma_T = 300$  ps, (d)  $\sigma_T = 200$  ps, (e)  $\sigma_T = 100$  ps, and (f)  $\sigma_T = 50$  ps. The solid line represents the  $K_L$  momentum to be less than 120 GeV/c, while dashed line for 50 GeV/c, half-dotted line for 20 GeV/c, and dotted line for 10 GeV/c.

$$\mathbf{K}_L \rightarrow \pi^0 \pi^0$$

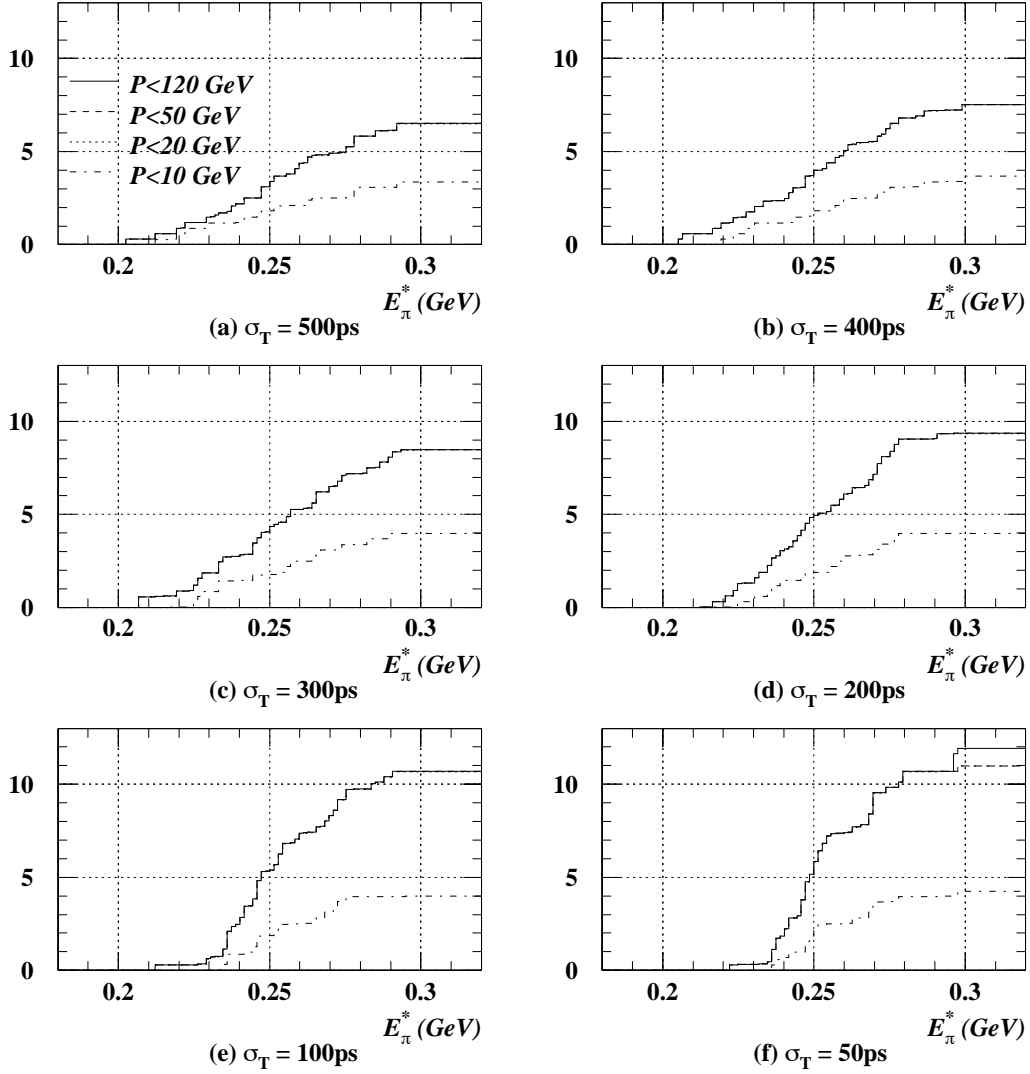


Figure 4.10: The number of events expected for  $K_L \rightarrow \pi^0 \pi^0$  for one year operation is shown as a function of the cut on  $E_\pi^*$  with photon veto counters of poorer performance. (a)  $\sigma_T = 500\text{ ps}$ , (b)  $\sigma_T = 400\text{ ps}$ , (c)  $\sigma_T = 300\text{ ps}$ , (d)  $\sigma_T = 200\text{ ps}$ , (e)  $\sigma_T = 100\text{ ps}$ , and (f)  $\sigma_T = 50\text{ ps}$ . The solid line represents the  $K_L$  momentum to be less than 120 GeV/c, while dashed line for 50 GeV/c, half-dotted line for 20 GeV/c, and dotted line for 10 GeV/c.

# Chapter 5

## Discussion

Based on the results obtained from the previous chapter, we will look at the effect of  $E_\pi^*$  cut and detector inefficiency. The relationship between kaon's initial momentum and  $E_\pi^*$  cut will also be discussed.

### 5.1 $E_\pi^*$ Cut

As the distributions in Figures 4.6 and 4.7 indicate, if we attain the level of time resolution,  $\sigma_T$ , to be 100 ps or 50 ps, sharp rise of the expected number of  $K_L \rightarrow \pi^0\pi^0$  events at around  $E_\pi^* = 250$  MeV appears. We may reduce the number of  $K_L \rightarrow \pi^0\pi^0$  events while maintaining the number of  $K_L \rightarrow \pi^0\nu\bar{\nu}$  events by imposing a  $E_\pi^*$  cut at this point.

In order to look for the optimum pion energy to make an effective cut, let us look at the poisson distribution. The poisson distribution can be expressed as

$$f_p(\mu, n) = \frac{\mu^n e^{-\mu}}{n!}, \quad (5.1)$$

which is the probability to observe  $n$  events while  $\mu$  events are expected. In order to establish a signal, the probability that the number of background events fluctuates up to the observed number of events should be sufficiently small. The probability that we observe  $N$  or more events while receiving  $\mu$  background events can be calculated as

$$P_p(\mu, N) = \sum_{n=N}^{\infty} f(\mu, n) = 1 - \sum_{n=0}^{N-1} f(\mu, n) \quad (5.2)$$

Figure 5.1 shows distributions of this probability where  $N$  is the sum of the numbers expected for  $K_L \rightarrow \pi^0\nu\bar{\nu}$  and  $K_L \rightarrow \pi^0\pi^0$  events.

According to Fig. 5.1, the  $P_p(\mu, N)$  keeps on decreasing as the  $E_\pi^*$  cut point is increased. This means that the best confidence level on the signal can be achieved without a cut on  $E_\pi^*$ .

## 5.2 Required Inefficiency and Resolution to Make Use of Time of Flight

Good efficiency of photon detection, both for signal detection and for background veto, is necessary to attain the signal sensitivity at the order of  $10^{-11}$  level. For this purpose, we must use as best detector components as possible. Effective use of  $E_\pi^*$  cut may compensate for the resource constraint to achieve required inefficiency and resolution level.

### 5.2.1 Inefficiency

Photon veto inefficiency is an important factor to suppress the background level. Figure 5.2 shows the energy distribution of gammas hitting each detector component for the  $K_L \rightarrow \pi^0\pi^0$  background events. A large contribution of  $K_L \rightarrow \pi^0\pi^0$  background level occurs due to high inefficiency of the PV and BA-In for small photon energies. Since the BA receives neutron hits, we can not reduce the BA-In inefficiency. Consequently, we need to suppress the number of  $K_L \rightarrow \pi^0\pi^0$  events by requiring the low PV inefficiency.

### 5.2.2 Time Resolution

As shown in distributions in Chapter 4, time resolution has a large effect on  $E_\pi^*$  reconstruction. Comparing the distributions in Figures 4.3 and 4.4, the FWHM of  $K_L \rightarrow \pi^0\pi^0$   $E_\pi^*$  peak has to be less than 40 MeV to clearly make a difference between  $K_L \rightarrow \pi^0\nu\bar{\nu}$  and  $K_L \rightarrow \pi^0\pi^0$ . This can be achieved when  $\sigma_T$  is 200 ps or lower, using high momentum of  $K_L$ . It is crucial to suppress  $\sigma_T$  less than at the level of 50 ps in order to make a  $E_\pi^*$  cut by utilizing the clear difference in  $E_\pi^*$  distribution between  $K_L \rightarrow \pi^0\nu\bar{\nu}$  and  $K_L \rightarrow \pi^0\pi^0$ .

For obtaining better time resolution of photomultipliers, we need high photo-electron output since the number of photo-electrons is statistically related to  $\sigma_T$  as

$$\sigma_T \propto \frac{1}{\sqrt{N_{pe}}} \quad (5.3)$$

where  $N_{pe}$  is the number of photo-electrons.

Shower fluctuation in the calorimeter also contributes to time resolution, since fluctuation in shower depth of CsI changes the arriving time of signal to the photomultiplier. This effect can be calculated by the following equation.

$$\sigma_x^2 = \int_0^\infty (x - \mu)^2 \frac{7}{9X_0} e^{-\frac{7x}{9X_0}} dx \quad (5.4)$$

where  $X_0 = 1.85cm$  is the radiation length of CsI and  $\mu$  is the average distance a shower can reach

$$\mu = \int_0^\infty x e^{-\frac{7x}{9X_0}} dx$$

$$= \frac{9X_0}{7}.$$

From equation (5.4), we can obtain  $\sigma_x = 2.38$  cm. This corresponds to the time fluctuation,  $\sigma_T^{shower}$  to be 143 ps.

Width of the beam bunch is also another factor to consider. The BNL collaboration expects the contribution of the bunch fluctuation should be around 100 ps [9].

Overall, we expect  $\sigma_T$  at KAMI cannot reach at the required level to make use of time of flight.

### 5.2.3 Energy Resolution

Even though contribution from energy resolution is small compared with time resolution, it indeed gives the fluctuation of  $E_\pi^*$  together with a fluctuation in  $z_{vtx}$ , as  $z_{vtx}$  is determined from the measurement of photon energy deposit on calorimeter.

From equation (3.1), the relation between the smearing effect of energy and vertex fluctuation can be shown as:

$$\frac{dz}{z_{CsI} - z_{vtx}} = \frac{1}{2} \sqrt{\sigma_{E_1}^2 + \sigma_{E_2}^2} \quad (5.5)$$

where  $\sigma_{E_1}$  and  $\sigma_{E_2}$  are the energy resolutions of the first and second photons in the calorimeter. If we suppose that  $E_1 = 9\text{GeV}$ ,  $E_2 = 1\text{GeV}$ , and the distance between the CsI calorimeter and the decay vertex to be 26 m, we can calculate  $\sigma_z = 35$  cm, by using equation (4.5) and (5.5). This is equivalent to the time resolution of 0.58 ps when we assume an average  $\beta$  of 0.9995 in our MC. Therefore, effect of energy resolution is negligible compared to time resolution.

## 5.3 $K_L$ Momentum

Although, high momentum beam of  $K_L$  in KAMI enables us to obtain relatively good gamma detection efficiency, the distribution of  $E_\pi^*$  has longer tail and makes the distinction between  $K_L \rightarrow \pi^0 \nu \bar{\nu}$  and  $K_L \rightarrow \pi^0 \pi^0$  more difficult.

When  $K_L$  momentum is less than 10 GeV, this long tail effect is more suppressed, especially in case of  $\sigma_T = 100\text{ps}$  or less, as can be seen in Fig. 4.3. However, it is difficult to gain signal acceptance for using such low momentum kaons. In fact, we can notice that  $K_L \rightarrow \pi^0 \nu \bar{\nu}$  events are more reduced by  $K_L$  momentum cut than  $K_L \rightarrow \pi^0 \pi^0$  events from the distributions in 4.6 and 4.7. Another problem for low momentum kaons arises because of the inefficiencies of veto counters. Lower initial momentum of kaons results in lower energy deposits of gammas in veto counters. Since inefficiencies of veto counters increase as the decrease of energy deposits, background events due to low energy of photons are not suppressed when we use low momentum of  $K_L$ 's. This situation is

illustrated in Figure 5.3. For these distributions,  $5 \times 10^5$   $K_L$ 's with monochromatic momenta, 4.0 to 4.3 GeV and 5.0 to 5.3 GeV, are generated. Three events in Figure (a) have weighted number of events corresponding to  $6 \times 10^{-6}$ . These three events all have 2 gamma hits on PV with lower energy range 0 and 20 MeV and upper energy range 400 MeV and 1 GeV. As shown in Figure (c), these events provide significant contributions to the calculated number of events expected for one year.

## 5.4 Feasibility of the time of flight measurement at KAMI

Time resolution is a major factor in smearing the distribution of pion energy in the  $K_L$  CMS, even with relatively long distance between the target and the decay region in the KAMI experiment. In order to effectively see the difference between  $K_L \rightarrow \pi^0 \pi^0$  and  $K_L \rightarrow \pi^0 \nu \bar{\nu}$ , we must have time resolution  $\sigma_T$  to be less than 50 ps. This is not achievable with the existing CsI due to a shower fluctuation. The energy resolution of CsI currently available is good enough for the time of flight measurement. Because there are many events in which high momentum  $K_L$  and time resolution gives  $\beta$  of  $K_L$  more than 1, the acceptance of signal events is sacrificed in the reconstruction of  $E_\pi^*$ .

As shown in the Poisson distribution in the beginning of this chapter, any cut of  $E_\pi^*$  does not effectively decrease the number of  $K_L \rightarrow \pi^0 \pi^0$  events while maintaining that of  $K_L \rightarrow \pi^0 \nu \bar{\nu}$ . Therefore, there is no advantage in using time of flight in the KAMI experiment.

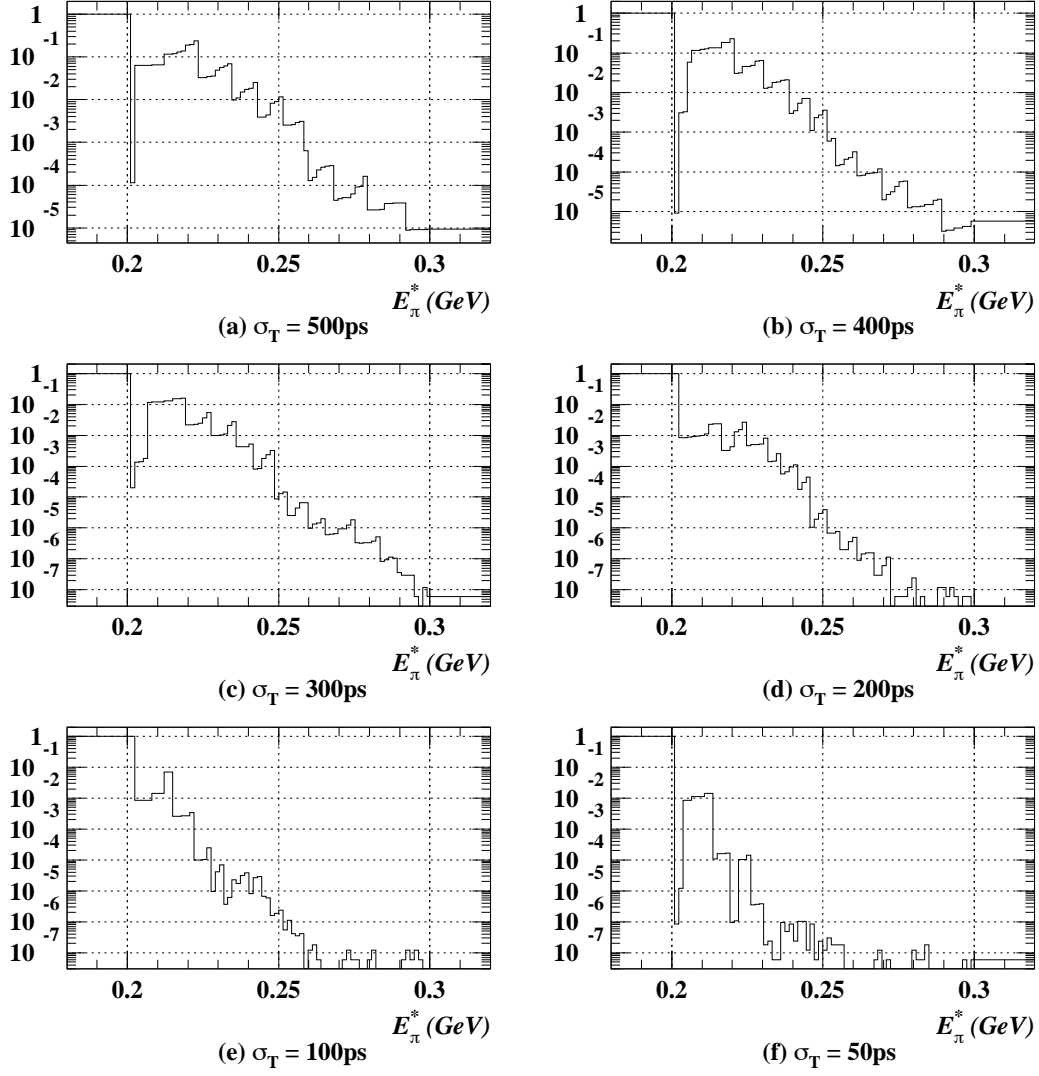


Figure 5.1: Probability that the  $K_L \rightarrow \pi^0 \pi^0$  background can fluctuate to more than the total number of  $K_L \rightarrow \pi^0 \nu \bar{\nu}$  and  $K_L \rightarrow \pi^0 \pi^0$ , is shown as a function of  $E_\pi^*$ . (a)  $\sigma_T = 500$  ps, (b)  $\sigma_T = 400$  ps, (c)  $\sigma_T = 300$  ps, (d)  $\sigma_T = 200$  ps, (e)  $\sigma_T = 100$  ps, and (f)  $\sigma_T = 50$  ps.

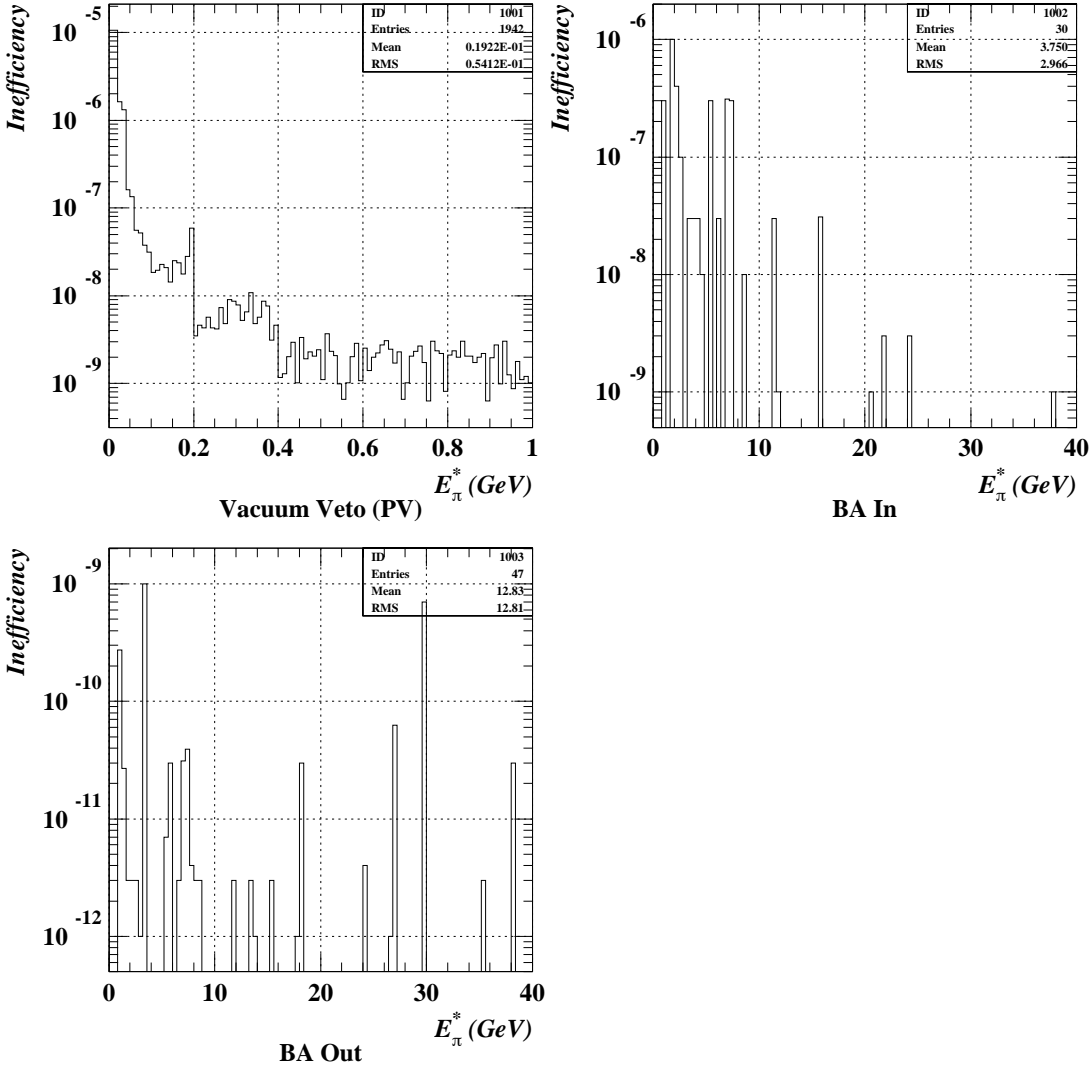


Figure 5.2: The probability that a low energy photon from the  $K_L \rightarrow \pi^0 \pi^0$  decay is not vetoed is shown. Energy distribution of gammas hitting (a) Vacuum Veto Counter (PV), (b) Back Anti-In, (c) Back Anti-Out, for the  $K_L \rightarrow \pi^0 \pi^0$  background events. The cuts described in Chapter 3 have been imposed.

$$\mathbf{K}_L \rightarrow \pi^0 \pi^0$$

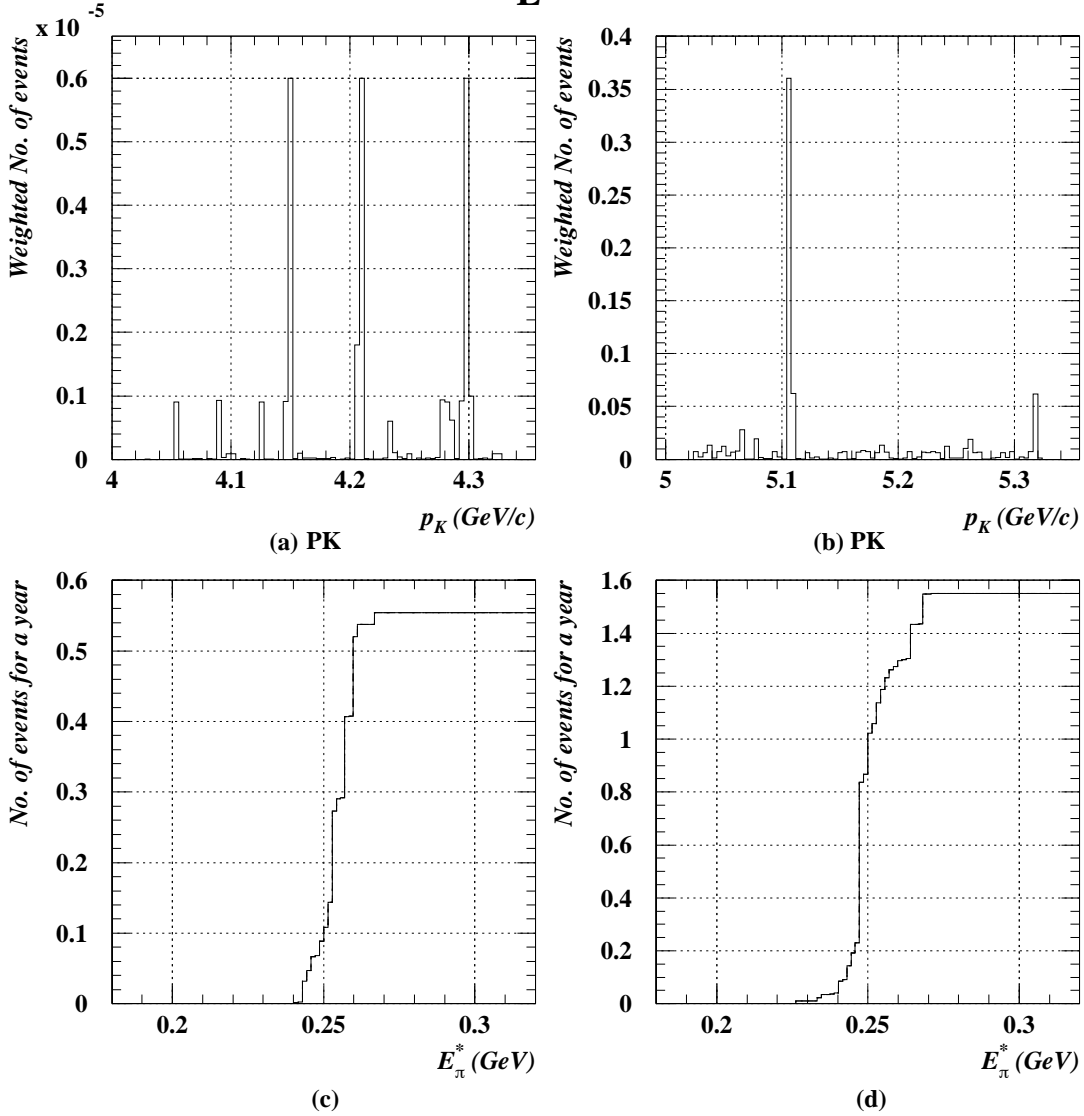


Figure 5.3: With low initial momentum,  $K_L \rightarrow \pi^0 \pi^0$  events appear due to low energy of photons. Figures (a) and (b) show the momentum distribution of initial  $K_L$ 's and weighted number of events. Figures (c) and (d) represent the corresponding number of accumulated events for one year, respectively.

# Chapter 6

## Conclusion

In order to detect  $K_L \rightarrow \pi^0 \nu \bar{\nu}$  at KAMI, use of the time of flight measurement is not effective to reduce background events. This is because the required  $\sigma_T$  of 50 ps does not seem to be achievable, and also the time of flight method provides no better signal to noise ratio than simply vetoing extra photons.

# Bibliography

- [1] J. Cronin, V. Fitch *et al.*, Phys. Rev. Lett. **13**, 138 (1964).
- [2] M. Kobayashi and T. Maskawa, Prog. Theor. Phys. **49**, 652 (1973).
- [3] L. Wolfenstein, Phys. Rev. Lett. **51**, 1945 (1983).
- [4] A. Buras, Phys. Lett. **B333**, 476 (1994).
- [5] G. Buchalla and A. Buras, Phys. Rev. **D54**, 6782 (1996).
- [6] T. Nakaya, Flavor Changing Neutral Current Conference, Santa Monica, CA (1997).
- [7] T. Inagaki *et al.*, KEK Proposal, Measurement of the  $K_L \rightarrow \pi^0 \nu \bar{\nu}$  decay (June, 1996).
- [8] M. Weaver *et al.*, Phys. Rev. Lett. **72**, 3758 (1994).  $K_L \rightarrow \pi^0 \nu \bar{\nu}$  (1997).
- [9] I-H. Chiang *et al.*, BNL proposal P926, Measurement of  $K_L \rightarrow \pi^0 \nu \bar{\nu}$  (Sept., 1996).
- [10] A. J. Malensek, FERMILAB-FN-0341 (1981).
- [11] K. Arisaka *et al.*, “An Expression of Interest to Detect and Measure the Direct  $CP$  Violating Decay  $K_L \rightarrow \pi^0 \nu \bar{\nu}$  and Other Rare Decays at Fermilab Using the Main Injector”, September 1997.